ELSEVIER

Contents lists available at ScienceDirect

Construction and Building Materials

journal homepage: www.elsevier.com/locate/conbuildmat





Experimental and numerical assessment of the bond behaviour of laser-cut reinforcement

Meisam Takalloozadeh a,c, Matthew Gilbert a, Dave Allen b, Giacomo Torelli a,*

- a Department of Civil and Structural Engineering, University of Sheffield, Sir Frederick Mappin Building, Mappin Street, Sheffield, S1 3JD, UK
- b Unipart Construction Technologies, Building 3, AMP Technology Centre, Brunel Way, Catcliffe, Sheffield, S60 5WG, UK
- ^c Department of Civil Engineering, School of Engineering, Shiraz University, Shiraz, Iran

ARTICLE INFO

Keywords: Bond strength Laser-cut reinforcement Reinforced concrete Pullout test Finite element analysis (FEA)

ABSTRACT

Reinforced concrete is a carbon-intensive technology, with concrete production contributing to 4%-8% of global CO₂ emissions, while steel production for reinforcement bars accounts for approximately 1.5% of global emissions. The use of concrete and steel in reinforced concrete can be minimized by optimizing the reinforcement layout and including reinforcing elements with variable cross-sections. This can be achieved through laser-cutting from steel sheet bespoke reinforcing elements that can then be assembled in optimized arrangements. However, a significant challenge in applying optimized laser-cut steel reinforcement is understanding the bond mechanisms between the reinforcement steel and the surrounding concrete to achieve composite behaviour. This study explores the bond behaviour of laser-cut reinforcement. A systematic experimental programme is designed to understand the effects of reinforcement geometry and surface treatment techniques on bond behaviour. Additionally, a numerical framework is developed to assess the mechanisms driving the transfer of bond stresses in the case of ribbed laser-cut reinforcement. The results indicate that incorporating ribs with appropriate spacing can increase the bond capacity by approximately six times in comparison to smooth laser-cut reinforcement, achieving a bond strength that falls between that of conventional smooth and ribbed rebars. The numerical results show that ribbed laser-cut reinforcement shares bond-stress transfer mechanisms with traditional ribbed rebars, with chemical adhesion and friction playing a significant role at low levels of slip, and mechanical interlocking dominating at higher slip levels. These findings have the potential to reduce material consumption through the use of optimized laser-cut steel reinforcement and provide a foundation for further optimizing the bond performance of laser-cut plates.

1. Introduction

Reinforced concrete is ubiquitous in the construction industry. However, one of the main issues with reinforced concrete is that it is a carbon-intensive construction system; the industrial production of concrete is responsible for 4%–8% of global $\rm CO_2$ emission [1], while the production of steel for reinforcement bars is associated with approximately 1.5% of global emissions [2].

Traditionally, a reinforced concrete element is realized by casting cylindrical steel rebars in concrete, with the rebars arranged in simple regular orthogonal configurations. A limitation of this traditional approach is that it will often lead to grossly under-utilized reinforcement and consequently excessive material consumption. Additionally, it is estimated that conventional methods of cutting rebar and arranging this into reinforcement cages typically leads to material waste of the order of 3 to 5% of the steel embedded in reinforced concrete [3]. If rebar of relatively large diameter is used, conventional methods

can lead to a material waste of the order of more than 10% [4]. An additional limitation of traditional reinforced concrete construction is that placement of the rebar is highly labour-intensive and errorprone. Traditional reinforcement is associated with high tolerances and variability, as it relies highly on the experience and skills of the labour. Furthermore, manual placement of the reinforcement raises significant health and safety concerns; according to Occupational Safety and Health Administration (OSHA), more than 60% of construction accidents take place when working with rebar [5].

The use of materials in reinforced concrete can be minimized by using optimized laser-cut steel plates as internal reinforcement; as an example, Fig. 1 shows an optimized reinforcement cage for a reinforced concrete slab. Using laser-cutting, constant-thickness steel sheets can be accurately cut into arbitrarily-shaped plates that can be subsequently assembled to achieve reinforcement cages with an optimized layout,

E-mail address: g.torelli@sheffield.ac.uk (G. Torelli).

Corresponding author.

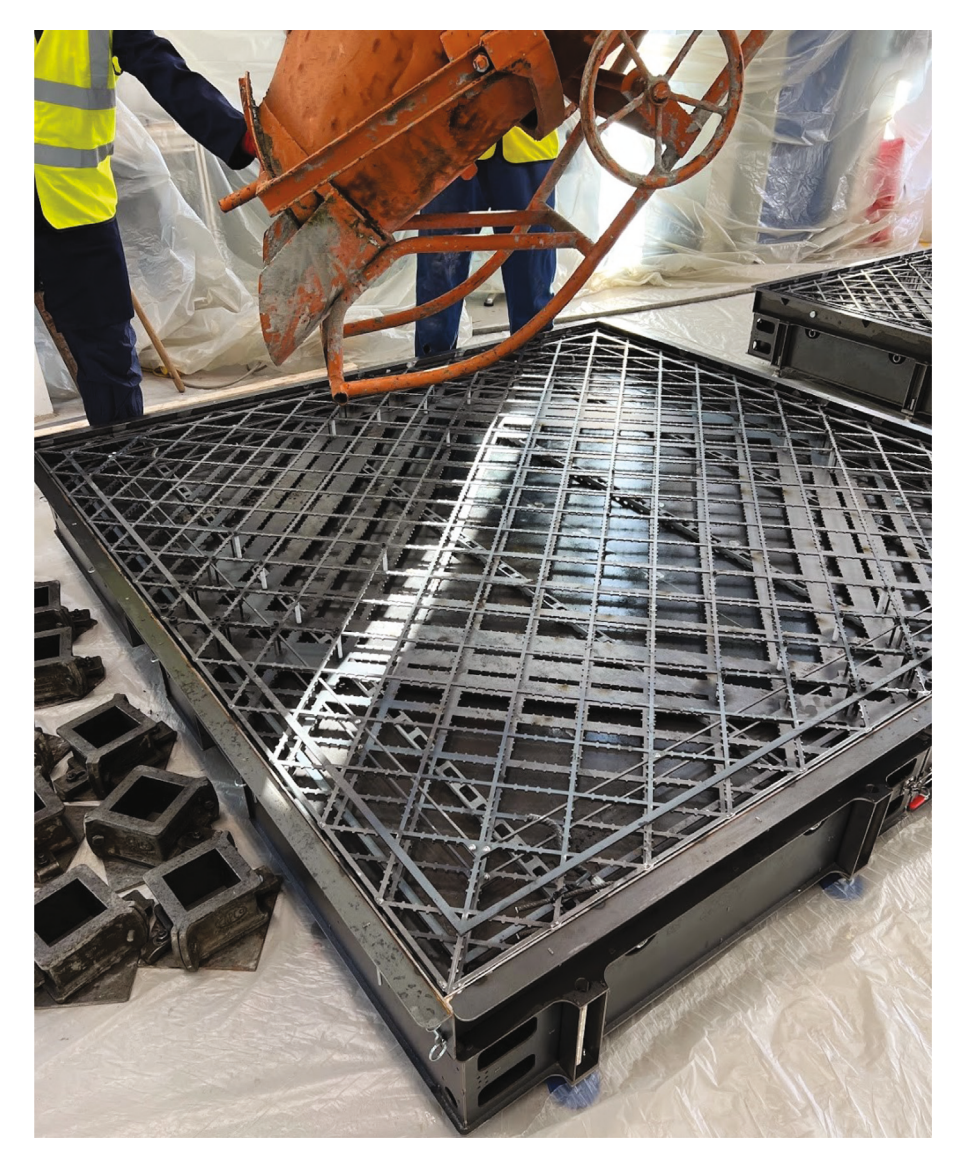


Fig. 1. Optimized LCR cage for a concrete slab.

leading to significant material savings to improve sustainability. Additional benefits of the technology are that (i) laser-cut profiles can be quickly assembled, boosting productivity, (ii) laser-cut tolerances increase geometrical precision, and (iii) the elimination of wire tying reduces health and safety risks.

However, a major challenge with Laser-Cut Reinforcement (LCR) is understanding the bond between reinforcement material and surrounding concrete. Indeed, the smooth flat surfaces of reinforcement that have been laser-cut from a metal plate can prevent effective stress transfer between steel and concrete, thus compromising the composite behaviour of a reinforced concrete element.

To date, comparatively few studies have sought to understand the bond behaviour of reinforcement formed from steel plates in concrete. Of these, experimental evidence suggests that steel plates can be used as a viable alternative to conventional shear and flexural reinforcement [6–9]. More recently, Sarahan et al. [10] investigated the bond behaviour of steel plates through the so-called beam-end method, a technique consisting of applying four-point bending to a concrete beam reinforced with a longitudinal element with a known bonded length [11]. These studies showed that the use of plates with a raised pattern on their surface (e.g., checker plates) can lead to a bond strength increase of up to 80% compared to smooth plates [10]. This demonstrates the potential to significantly boost the performance

of laser-cut steel through the use of optimized geometrical features. However, a systematic assessment of the effects of geometrical features and surface-roughening treatments is required to build understanding and to ensure optimal performance of laser-cut steel reinforcement.

To address this, the present work makes a major contribution to the wider use of optimized low-carbon laser-cut reinforcement by quantifying the bond performance of laser-cut steel and investigating its dependency on plate geometry and surface treatment techniques. Specifically, a total of 48 pullout tests are performed to (i) identify the effects of plate thickness and plate width, and (ii) explore the potential of boosting the bond strength with bond-enhancing geometrical features (ribs and holes) and surface-roughening treatments. Additionally, a numerical simulation framework is developed to shed light on the mechanisms driving the bond behaviour of ribbed LCR, providing the necessary understanding to allow further optimization of elements that include LCR. The framework is validated against experimental results so that it can be used with confidence to support the development of bespoke LCR systems.

The paper is organized as follows: test methods and results are detailed in Sections 2 and 3 respectively, while Section 4 presents details of the proposed numerical framework; finally, conclusions are drawn in Section 5.

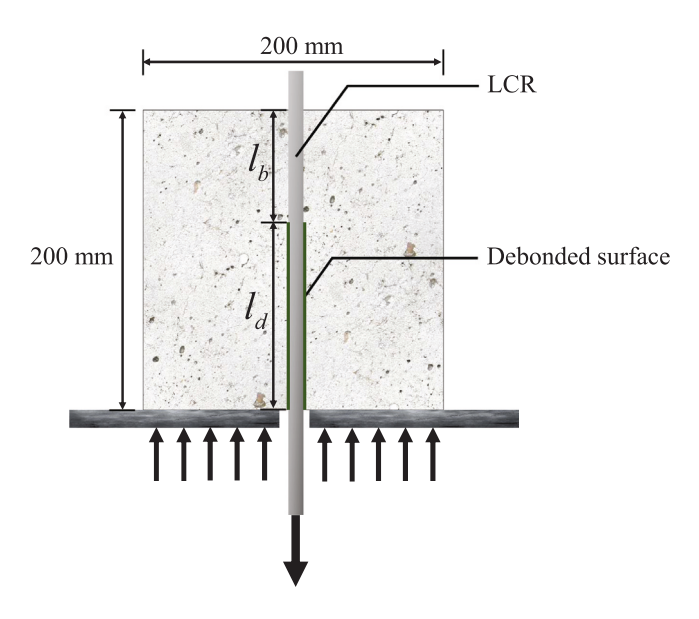


Fig. 2. Pullout test setup.

2. Experimental programme

Four series of pullout experiments were performed to investigate the effects of (i) plate width, (ii) geometric features (ribs and holes) and surface-roughening treatments, (iii) ribs spacing and (iv) plate thickness. The four series are denoted S1 to S4, respectively.

The LCR configurations considered herein were embedded in a concrete cube with 200 mm side length and tested in the pullout, as schematized in Fig. 2. Specifically, 14 different configurations of laser-cut steel plates, denoted T1 to T14, were tested. These include plates with various geometrical and surface treatment features; see the overview provided in Fig. 3, which also shows the test series (S1 to S4) in which each configuration was studied. To characterize the variability of bond behaviour, and to minimize the effects of outliers or anomalies, hence achieving a reliable representation of bond behaviour, for each configuration three identical repeat specimens were manufactured and tested. The notation used to identify each specimen is as follows: <Test series ID><Configuration ID><Repeat ID>. For example, specimen S1T2R3 refers to the third test repeat on configuration T2 (see Fig. 3), performed within test series S1 (concerned with the effects of plate width).

An overview of the test series, configurations, and tested specimens is provided in Table 2. For configuration T10, three additional tests were performed under confined conditions within test series 3, to avoid splitting and invoke a slip failure mode. Furthermore, three additional configuration T10 specimens were tested within test series S4, resulting in 48 pullout tests overall. Fig. 3 provides an overview of the four test series and all the individual tests performed.

To promote slip failure and avoid yielding of the steel, bond stresses were concentrated in a limited portion of the lateral surface of each plate. This was achieved by intentionally de-bonding part of the lateral surface (see Fig. 3). The de-bonded lateral surface was wrapped with several layers of cling film prior to concrete casting to ensure no contact between the plate and concrete (Fig. 4). The adopted bonded length l_b for the first and second test series was equal to five times the width w of the plate. This choice was based on existing evidence and guidelines for pullout tests on circular section rebars, where a bonded length equal to five times the rebar diameter is recommended to achieve slip failure without steel yielding [12,13]. However, based on the split failures observed in the present study for a bond length l_b equal to five times the width w, the bonded length has been reduced to 75 mm for the third and fourth test series. This ensured that slip failure occurred without

steel yielding or concrete splitting. It is worth noting that the bonded length might also have an effect on the distribution of equivalent tangential stresses along the bonded surface itself, with longer bonded lengths deviating from the ideal case of constant equivalent tangential stresses

Details of test configurations, materials and test setup are provided in the following sections.

2.1. Specimens preparation

As discussed above, four test series were designed to investigate the effects of (i) plate width, (ii) geometric features (ribs and holes) and surface-roughening treatments, (iii) spacing between bond-enhancing ribs, and (iv) plate thickness.

2.1.1. Series S1: varying plate width

The first series (S1) aimed to establish the relationship between plate width and bond behaviour for prismatic laser-cut strips. Specifically, the series studied the behaviour of 3 mm thick strips with widths of 10, 20, and 30 mm respectively. The IDs of the tests conducted within this series are shown in Table 2 (see specimens S1T1R1 to S1T3R3). The geometry of the corresponding configurations T1 to T3 is shown in Fig. 3.

2.1.2. Series S2: geometric features and surface-roughening treatments

The second test series (S2) investigated the effects of surface coating, surface roughening, perforations, ribs and the combined effects of perforations and ribs (see schematic of configurations T4 to T8 in Fig. 3, photos of the realized plates in Fig. 4 and details of the resulting specimens S2T4 to S2T8 in Table 2).

For configuration S2T4, a rough surface was achieved by applying a layer of steel primer with an approximate thickness of 0.25 mm. Specifically, the adopted primer was *Rockbond* steel primer manufactured by Rockbond SCP Ltd, which is a commercial product incorporating micro silica cement and fine Portland cement, along with an elastomeric acrylic co-polymer resin powder and a combination of compatible admixtures. By contrast, for configuration S2T5 a rough surface was obtained through indentations generated via laser beam. The indentation pattern was defined by selecting an offset pitch of 2.5 mm across the surface (see the pattern in Fig. 4). Finally, perforated (S2T6), ribbed (S2T7), and simultaneously ribbed and perforated plates (S2T8) were obtained via direct laser-cutting of steel sheets. The geometries of these specimens, including details of ribs and holes, are reported in Fig. 3 (see configurations T6, T7 and T8, as well as details A and B).

2.1.3. Series S3: varying ribs spacing

The third series of experiments (S3) investigated the relationship between rib spacing and bond performance in ribbed plates; see details of configurations T9 to T11 in Fig. 3. Specifically, rib spacings of 36 mm, 18 mm, and 9 mm were adopted for specimens S3T9, S3T10 and S3T11 respectively. To obtain directly comparable results, the bonded length was kept consistent across all specimens in the series. In light of the splitting failure observed in all the test repeats for the specimens with a rib spacing of 18 mm (see repeats S3T10R1 to S3T10R3 in Table 2), three additional test repeats were conducted under confined conditions (see repeats S3T10R4 to S3T10R6 in Table 2). For these specimens, an increased level of concrete confinement was achieved by using a reinforcing cage comprising four closed-loop stirrups, each with a diameter of \$\phi 6\$ mm as illustrated in Fig. 5. This choice was based on previous research studies that demonstrated that adequate transverse reinforcement can be adopted to achieve slip failure [14,15]. Note that the stirrups were positioned in the portion of the cube where splitting cracks were experimentally shown to originate. Although increasing the compressive/tensile strength of the concrete could be an alternative approach to promote slip failure, providing lateral confinement while keeping a constant mix composition was deemed a more suitable method for achieving directly comparable results.

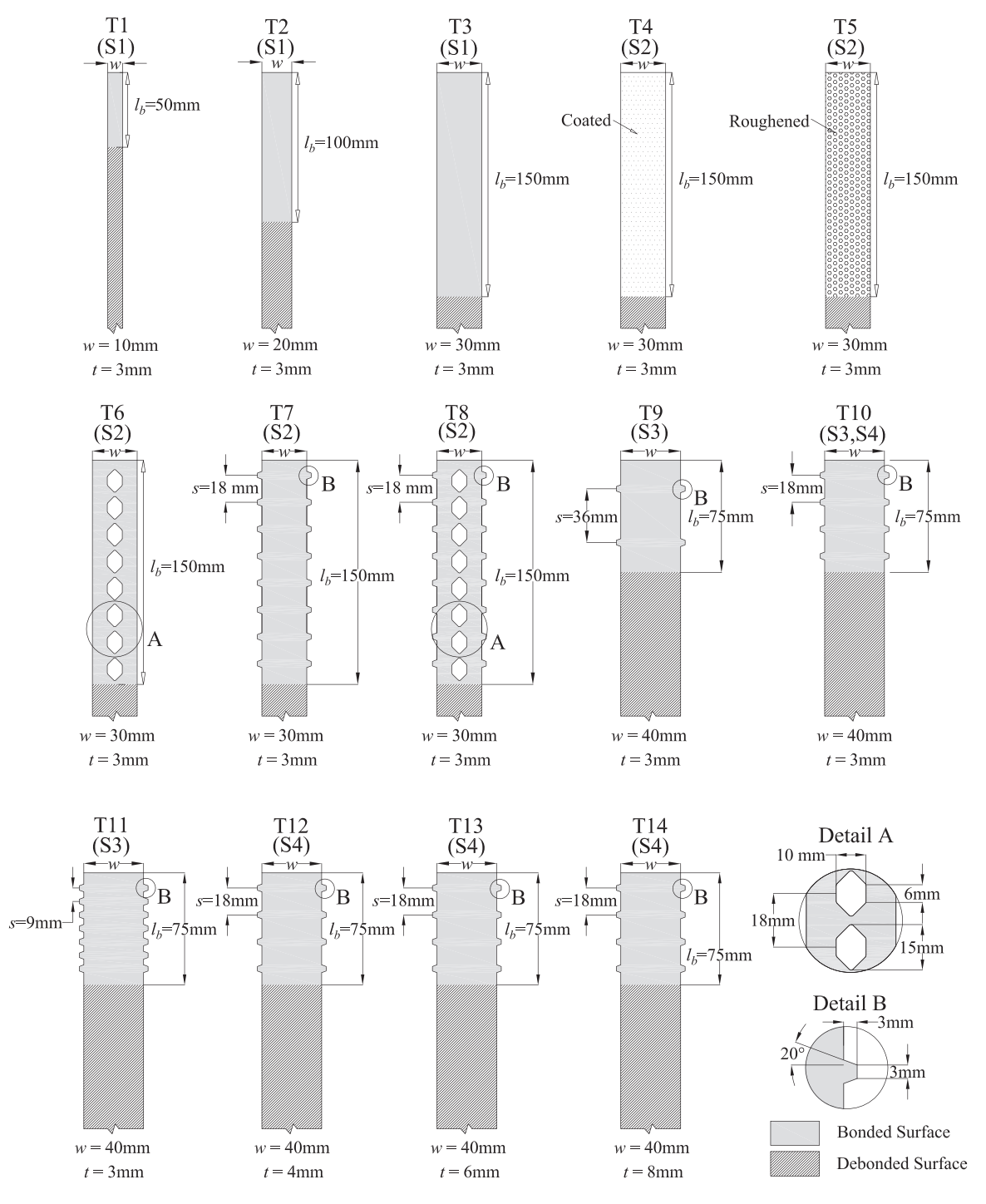


Fig. 3. Geometry of the LCR configurations (T1 to T14) adopted in the test series (S1 to S4), detailing plate width w, plate thickness t, bonded length l_b and rib spacing s. Note that the plate thickness, as specified for each configuration, is constant along the bar.

Table 1 Mix compositions and design density of the individual constituents (Superplasticizer content equivalent to 1.6% of cement mass).

Constituent	Density [kg/m³]	Amount [kg/m³]			
Water	1000	180			
Cement CEM II-A-LL 32.5R	3100	300			
Fine Aggregate	2625	835			
Coarse Aggregate (4-10 mm)	2625	1015			
Superplasticizer	1000	4.8			

2.1.4. Series S4: varying plate thickness

The final test series, S4, was designed to investigate the impact of the thickness of the ribbed LCR plate on its bond behaviour. Ribbed LCR with thicknesses of 3, 4, 6, and 8 mm were tested, all of which had a rib spacing of 18 mm (see details of configurations T12 to T14 in Fig. 3). This rib spacing was chosen because it was found to yield the highest bond strength of all the spacings tested in the previous series. As undertaken for tests S3T10R4 to S3T10R6 (see Section 2.1.3), all the tests within series S4 included three closed-loop stirrups with a diameter of $\phi 6$ mm (see Fig. 5) to increase the level of confinement in order to induce slip failure.

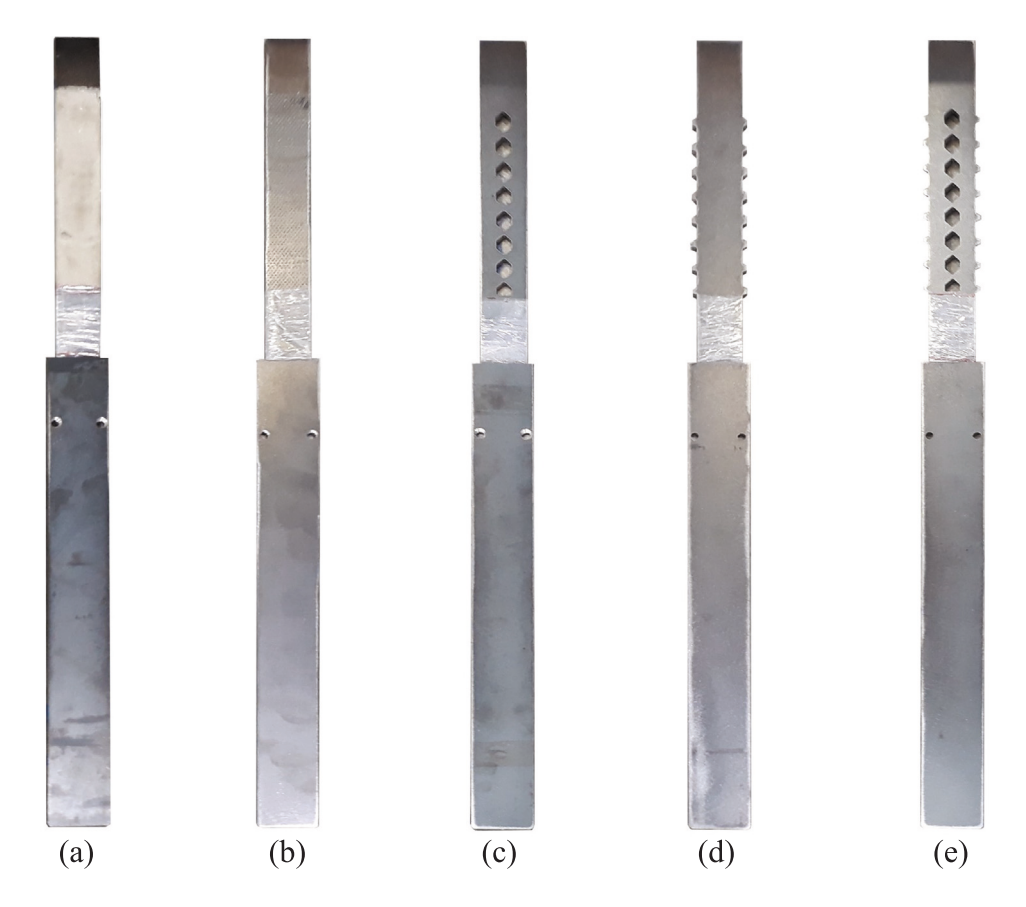


Fig. 4. Configurations studied in series S2: (a) T4 — Coated surface, (b) T5 — Roughened surface, (c) T6 — Perforated, (d) T7 — Ribbed, and (e) T8 — Perforated and ribbed.

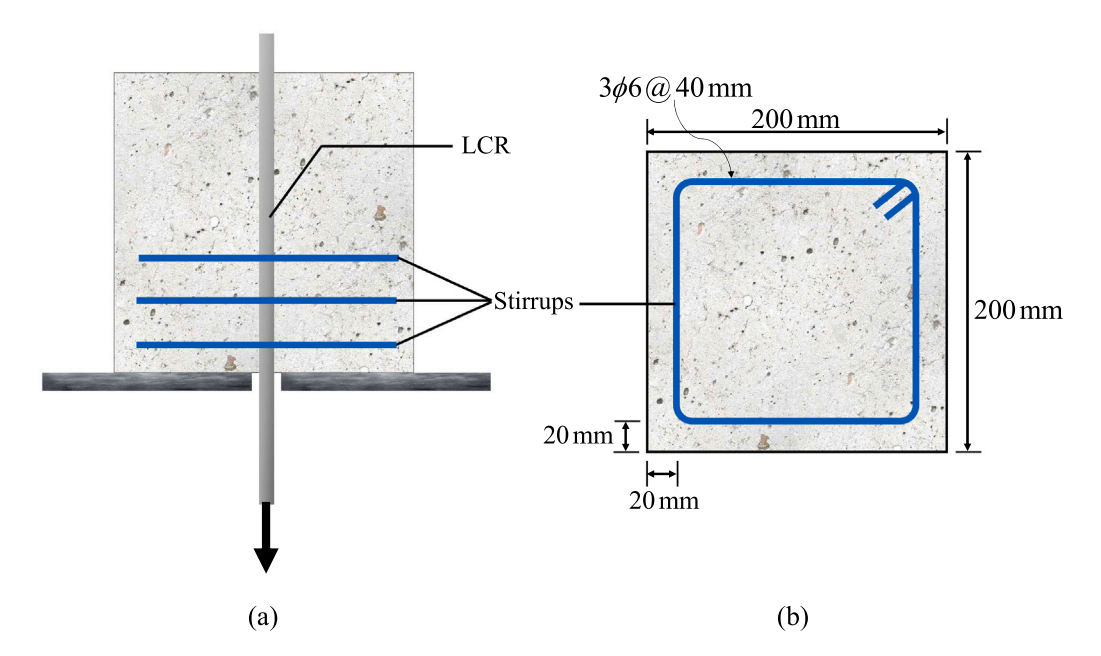


Fig. 5. Details of the stirrups adopted for tests with increased confinement (S3T10R4 to S3T10R6 and S4T10R1 to S4T14R3): (a) vertical section, and (b) horizontal section.

2.2. Materials

The plates were laser-cut out of sheets of S355 steel, a structural grade steel with a minimum yield strength of 355 $\rm N/mm^2$. To obtain directly comparable results, the same concrete mix design was adopted for all tests. Table 1 shows the composition of the adopted mix. The mix employed a CEM II/A-LL standard Portland-limestone cement with a

strength grade of 32.5R, in accordance with the regulations of European Standard EN 197-1 [16]. The adopted mix was selected to achieve concrete strength classes representative of practical applications. The sand used had a maximum particle diameter of 4 mm while the gravel had a maximum diameter of 10 mm. In order to attain adequate levels of workability, a high-range PCE superplasticizer, in compliance with European Standard BE 934-2 [17], was used.

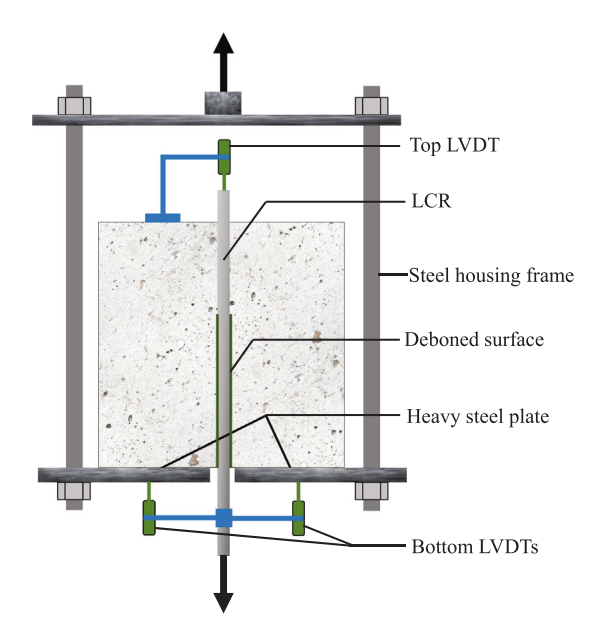


Fig. 6. Test setup: housing frame, applied load and strain measuring devices.

2.3. Test method

Various experimental methods have been developed over the years to assess the bond behaviour of steel reinforcement embedded in concrete, including the beam–column joint test [18], the beam anchorage test [19], splice-beam test [20], the beam-end test [11] and the direct pullout test [21,22]. The present study employs the pullout test, widely used owing to its simplicity, repeatability and applicability to various reinforcement configurations [23]. The method involves applying a tensile force to a steel reinforcement bar embedded in concrete and measuring the force required to pull the bar out. The bond strength (τ) is then obtained by dividing the maximum applied load by the bonded lateral surface of the reinforcing member. Fig. 6 shows the pullout test setup employed in this study.

2.4. Test apparatus

The test apparatus employed in this study is illustrated in Fig. 7. The loading rig is a universal uniaxial testing machine with a capacity of 300 kN. The primary hydraulic actuator in the machine is positioned at the centre of a cross-head and connected to a steel plate. Another steel plate of equal thickness is linked to this plate through four bars, forming a frame that encloses the concrete block. The concrete block with embedded LCR is positioned within this housing frame. The part of the LCR that extends from the block is inserted into a slot in the bottom steel plate, and its end is secured by the self-reacting frame of the machine using a clamp connection.

The load is applied under controlled displacement conditions, with a displacement rate of 0.5 mm/min for displacements up to 4 mm and a rate of 1 mm/min thereafter.

Three Linear Variable Differential Transformers (LVDTs) were utilized to measure relative displacements between the concrete and LCR (see Figs. 6 and 8). Specifically, one LVDT was placed at the top of each concrete cube to measure the relative displacement between the free end of the plate (that is, the non-loaded end) and the concrete block (see Fig. 8(a)). To measure relative displacements at the loaded end of the plate, two additional LVDTs were mounted on either side of the bottom plate (see Fig. 8(b)). Two LVDTs were used to enable detection of any eccentricity in the pullout setup. As shown in Fig. 8(b), a custom cast acrylic attachment was employed to connect the two lower LVDTs to the protruding section of LCR. Specific holes were drilled in

the bottom plate to facilitate contact between the two lower LVDTs and the concrete. Throughout the tests, applied loads and machine displacements were also continuously monitored and recorded.

3. Test results

3.1. Overall findings

Table 2 summarizes the results of the four test series. For each individual test, the table reports the maximum pullout force, the maximum tensile stress in the plate, bond stress at the onset of slip of the free end of the plate, the bond strength, the observed failure mode (i.e., splitting (SP) or slipping (SL)), the slip recorded at the loaded end of the plates when the maximum bond stress is reached (δL , obtained as the average of the reading of the two bottom LVDTs depicted in Fig. 8), and the slip recorded at the free end of the plates when the maximum bond stress is reached (δU). "Slipping failure" here refers to an inadequate bond between rebar and concrete, leading to rebar slippage. "Splitting failure", on the other hand, refers to the development of cracks in the concrete around the rebar, in the radial direction, leading to a split of the concrete cube itself. Table 2 also summarizes the average bond strength, bond strength standard deviation (STD), bond strength coefficient of variation (CoV), and average concrete strength for three specimens in each configuration. The bond stress was determined by dividing the pullout load by the nominal surface area of the bonded portion of the plate. The displacement at the loaded end of each specimen was computed as the difference between the measured displacement and the elastic deformation of the laser-cut plate.

It is evident from the results presented in Table 2 that the majority of the tested specimens failed by slipping, thus giving a valuable insight into the bond behaviour of the given test configuration. As anticipated, the concrete cubes provided adequate confinement and effectively restrained the plates, enabling them to achieve their highest bond strength and preventing the occurrence of radial cracks and subsequent splitting. However, premature failure was observed for configurations with bond-enhancing lateral ribs (configurations S2T7, S3T10), where the enhanced bond performance offered by the lateral ribs meant that splitting failure occurred prior to the bond capacity of the plates being reached. As previously mentioned, in order to assess the actual bond strength offered by bond-enhancing lateral ribs, three additional tests were performed within series S3 using additional confinement to ensure slip failure was induced (see results obtained for specimens S3T10R4 to S3T10R6).

Table 2 shows that the bond strength CoV obtained for each configuration is generally of the order of 20% or lower. This is in line with the expected variability of the concrete strength parameters [24], indicating acceptable levels of variability. Fig. 9 shows the same results graphically, showing the bond strength obtained for each test and grouping results by test series. In the case of tests S3T10, Fig. 9(c) reports the bond strength obtained both with (specimens S3T10R4 to S3T10R6, all failing by slip failure) and without lateral confinement (specimens S3T10R1 to S3T10R3, all failing by splitting).

In Figs. 10–14 sample bond stress-slip curves obtained for all the configurations tested in each test series are presented, with the first test repeat (R1) was selected for each configuration. Fig. 13 also shows the result of the fourth repeat for configuration T10 (i.e., test S3T10R4) to illustrate the effects of stress confinement (only present in tests S3T10R4 to S3T10R6 — see Section 2.1). These results are discussed further in the following sections.

Fig. 15 shows the same results graphically, showing the normalized average bond strength obtained for each test configuration and the corresponding standard deviation. Note that the average bond strength was normalized by concrete compressive strength in order to remove the effects of concrete strength variations, thereby facilitating more direct comparison between the bond performance offered by the various configurations. Normalized values were obtained by dividing the



Fig. 7. Test apparatus: universal testing machine and pullout test assembly.

bond strength by the square root of the compressive strength, rather than by directly dividing by the concrete compressive strength. This normalization approach was selected in light of the well-known nonlinear relationship between bond strength and concrete strength, which is commonly captured by assuming the bond strength to be proportional to the square root of the compressive strength (see e.g., [25]). Since the values of concrete compressive strength obtained for the various concrete batches did not vary significantly across the whole test programme (see values reported Table 2), the normalized bond strength

values reported in Fig. 15 exhibit the same trends as the observed bond capacities (see Fig. 9).

3.2. Detailed findings

3.2.1. Series S1: effects of plate width

All the specimens tested in series S1 (prismatic laser-cut strips) exhibited slip failure. As expected, due to the smooth surfaces of the strips, the observed bond strength was in the same range as the bond



Fig. 8. LVDT displacement gauges measuring the relative displacements between concrete and steel: (a) top LVDT, located at the free end of the plate, and (b) bottom LVDTs, located at the loaded end of the plate.

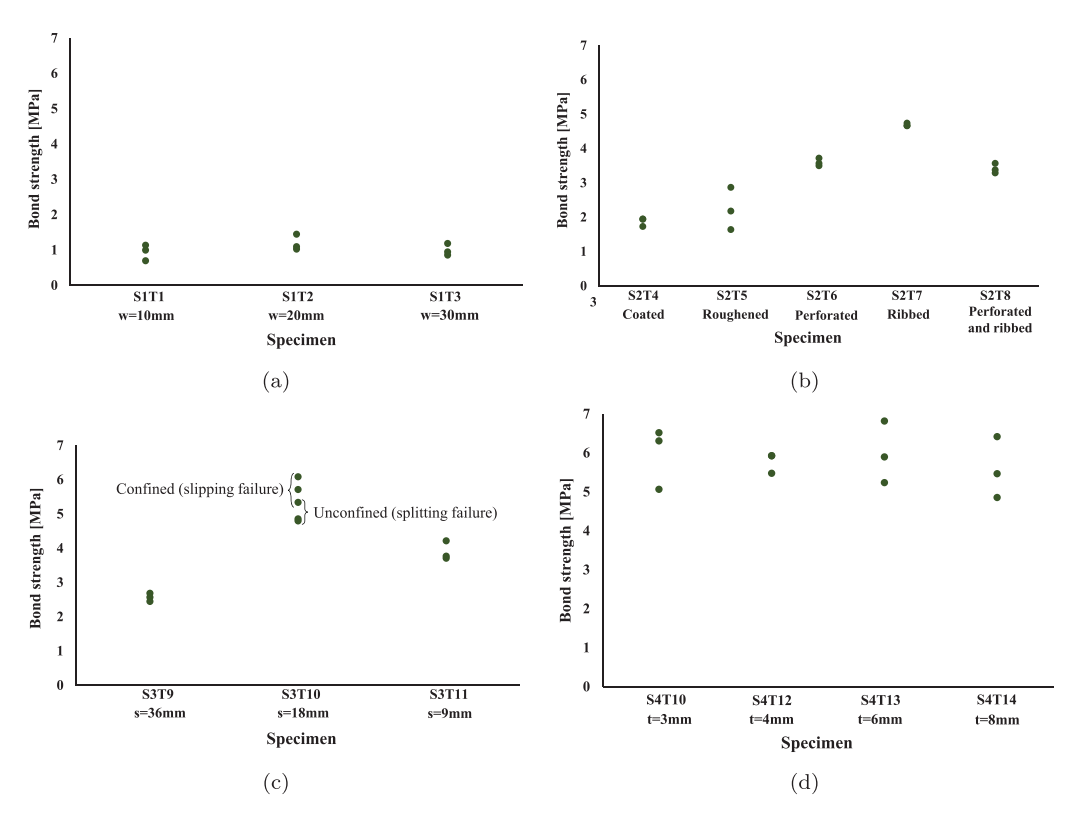


Fig. 9. Overview of bond strength results grouped by test series (a) S1, (b) S2, (c) S3 and (d) S4.

strength typically exhibited by conventional smooth rebars, with values hovering around 1 MPa; see the bond strength values obtained for specimens S1T1, S1T2 and S1T3 in Table 2.

As can be seen graphically in Fig. 9(a), the results indicated that the bond strength was not significantly affected by the width of the

prismatic laser-cut strips. That is, the bond capacity of a given plate seems to grow approximately linearly with its width w. This can be explained by the fact that chemical adhesion and friction offer shear stresses that are approximately proportional to the contact area.

Table 2
Overview of test series, specimen IDs and results

Test series	Varying feature	Bar conf.	Feature	Specimen ID	Stirrup Confin- ement	Max. Force [kN]	Max. Tensile stress [MPa]	Slip bond stress [MPa]	Bond strength [MPa]	Failure mode	δL [mm]	δ <i>U</i> [mm]	Average bond strength [MPa]	STD (Bond strength) [MPa]	CoV (Bond strength) (%)	Concrete strength [MPa]
S1	Plate width (w)	T1	w = 10 mm	S1T1R1 S1T1R2 S1T1R3	No No No	1.48 1.30 0.91	49 43 30	1.14 0.83 0.65	1.14 1.00 0.70	SL SL SL	0.05 0.20 0.18	0.03 0.20 0.17	0.95	0.22	23.7	29.2
		T2	w = 20 mm	S1T2R1 S1T2R2 S1T2R3	No No No	4.74 5.06 6.67	79 84 111	0.84 1.10 1.31	1.03 1.10 1.45	SL SL SL	0.07 0.00 0.11	0.04 0.01 0.00	1.19	0.23	18.9	28.5
		Т3	w = 30 mm	S1T3R1 S1T3R2 S1T3R3	No No No	11.78 9.41 8.51	131 105 95	1.10 0.95 0.86	1.19 0.95 0.86	SL SL SL	0.16 0.09 0.06	0.06 0.03 0.00	1.04	0.20	19.6	28.0
S2 features and surface- rougheni		T4	Coated	S2T4R1 S2T4R2 S2T4R3	No No No	19.21 17.13 19.31	213 190 215	1.94 1.60 1.95	1.94 1.73 1.95	SL SL SL	0.16 0.26 0.17	0.00 0.00 0.13	1.87	0.12	6.6	36.8
		Т5	Roughened	S2T5R1 S2T5R2 S2T5R3	No No No	21.58 16.24 28.41	240 180 316	1.20 - 2.10	2.18 1.64 2.87	SL SL SL	1.11 - 0.97	0.00 0.00 0.53	2.23	0.62	27.6	35.1
	and	т6	Perforated	S2T6R1 S2T6R2 S2T6R3	No No No	34.65 35.34 36.83	385 393 409	2.55 2.65 2.82	3.50 3.57 3.72	SL SL SL	2.70 2.90 1.46	0.00 0.21 0.21	3.60	0.11	3.1	37.6
	roughening treatments	T7	Ribbed (s = 18 mm)	S2T7R1 S2T7R2 S2T7R3	No No No	46.93 46.23 46.13	521 514 513	3.48 3.50 3.57	4.74 4.67 4.66	SP SP SP	- 3.76 3.47	0.00 0.71 0.64	4.69	0.04	0.9	32.5
		т8	Perforated and ribbed	S2T8R1 S2T8R2 S2T8R3	No No No	35.34 33.46 32.57	393 372 362	- 2.65 2.60	3.57 3.38 3.29	SL SL SL	2.19 2.69 2.70	0.00 0.00 0.00	3.41	0.14	4.2	36.7
\$3	Ribs spacing (s)	Т9	s = 36 mm	S3T9R1 S3T9R2 S3T9R3	No No No	15.80 17.35 16.58	132 145 138	2.24 2.10 1.88	2.45 2.69 2.57	SL SL SL	3.28 0.66 4.76	3.57 0.94 5.07	2.57	0.12	4.7	33.2
		T10	s = 18 mm	S3T10R1 S3T10R2 S3T10R3	No No No	34.44 30.96 31.35	287 258 261	3.05 3.40 3.50	5.34 4.80 4.86	SP SP SP	3.44 2.37 2.50	3.96 2.79 2.60	5.00	0.30	5.9	32.3
				S3T10R4 S3T10R5 S3T10R6	Yes Yes Yes	39.28 36.86 46.46	327 307 387	3.00 2.80 2.90	6.09 5.71 7.20	SL SL SL	3.47 5.53 5.63	3.59 5.57 9.46	6.34	0.77	12.2	31.0
		T11	s = 9 mm	S3T11R1 S3T11R2 S3T11R3	No No No	24.32 23.93 27.22	203 199 227	3.77 3.50 4.22	3.77 3.71 4.22	SL SL SL	0.45 1.24 0.48	1.21 1.35 0.83	3.90	0.28	7.1	31.1
\$4	Plate thickness (t)	T10	t = 3 mm	S4T10R1 S4T10R2 S4T10R3	Yes Yes Yes	42.05 32.70 40.70	350 273 339	3.91 3.35 3.90	6.52 5.07 6.31	SL SL SL	4.41 4.10 8.89	5.06 4.50 9.29	5.97	0.78	13.1	26.7
		T12	t = 4 mm	S4T12R1 S4T12R2 S4T12R3	Yes Yes Yes	39.14 36.17 39.14	245 226 245	3.05 3.20 2.90	5.93 5.48 5.93	SL SL SL	6.08 3.47 5.74	6.45 3.80 6.34	5.78	0.26	4.5	25.9
		T13	t = 6 mm	S4T13R1 S4T13R2 S4T13R3	Yes Yes Yes	47.06 35.95 40.71	196 150 170	3.20 2.80 3.35	6.82 5.21 5.90	SL SL SL	3.05 3.64 4.81	3.71 3.94 5.31	5.98	0.81	13.5	27.8
		T14	t = 8 mm	S4T14R1 S4T14R2 S4T14R3	Yes Yes Yes	46.22 39.38 34.99	144 123 109	4.80 4.20 3.60	6.42 5.47 4.86	SL SL SL	3.80 6.07 4.22	4.38 6.67 4.79	5.58	0.79	14.1	27.1

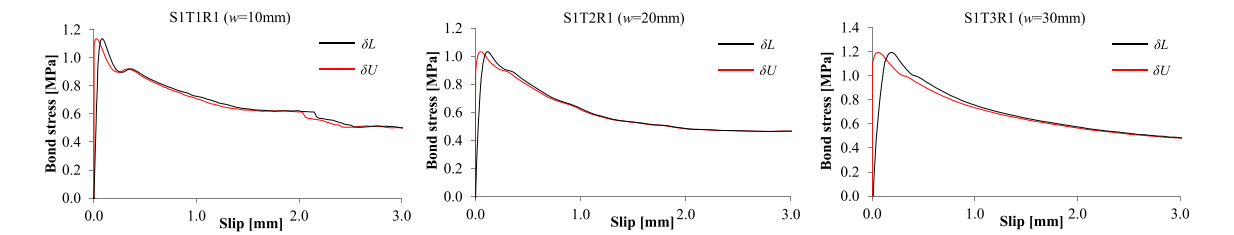
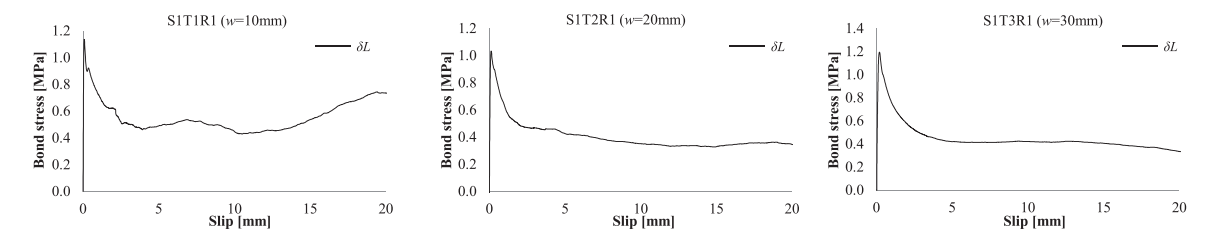


Fig. 10. Stress-slip curves for series S1 plotted for slips up to 3 mm.



 $\textbf{Fig. 11.} \ \ \textbf{Stress-slip} \ \ \textbf{curves} \ \ \textbf{for test series} \ \ \textbf{S1}.$

Fig. 10 shows the stress-slip curves obtained for configurations T1, T2 and T3, plotted based on the slip of the loaded end (δL) and the slip of the free end (δU), for slips up to 3 mm. These curves show that the loaded end is always mobilized first. This indicates that slipping of the loaded end initiates early during the loading process, immediately after

the chemical adhesion between the plate and concrete is disrupted. Subsequently, the primary factor influencing bond resistance is the friction between the plate and concrete along the bonded section. On the other hand, the slip at the free end remains negligible until the adhesion is completely lost over the entire embedded length.

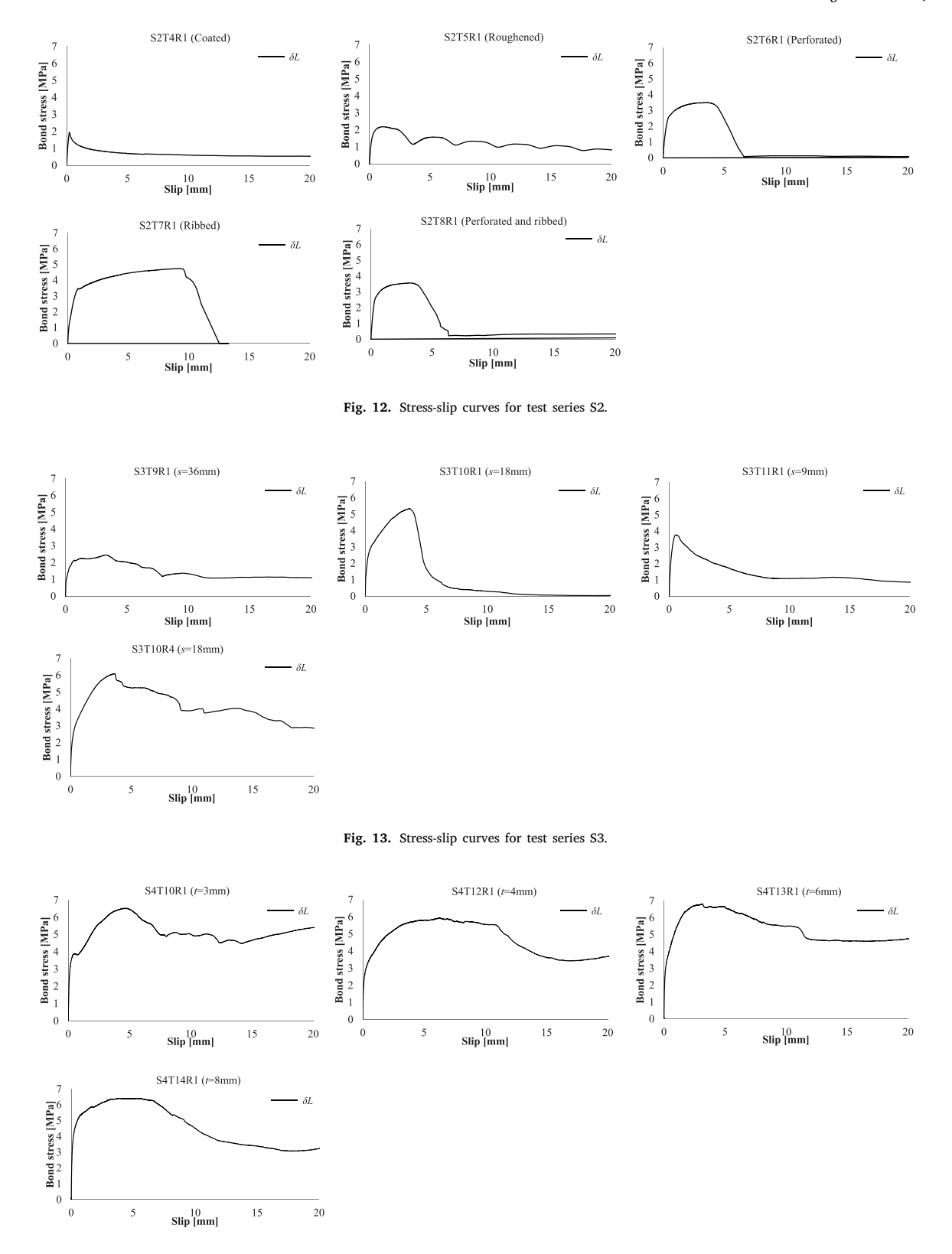


Fig. 14. Stress-slip curves for test series S4.

Fig. 11 shows the stress-slip curves for slips up to 20 mm, based on the slip of the loaded end only. The figure shows that the examined prismatic laser-cut strips exhibit a relatively brittle behaviour, with residual bond stresses of the order of 50% of the bond stress for a slip of 10 mm. However, the curves reported in Fig. 11 also show that such residual bond stress does not decrease significantly for slips larger

than 10 mm, possibly due to a sustained friction effect in this region. Specifically, for slips larger than 10 mm, the residual bond stresses are either approximately constant (see curves obtained for test S1T2R1 and S1T3R1, in Fig. 11) or progressively increasing (see curves obtained for test S1T1R1 in Fig. 11).

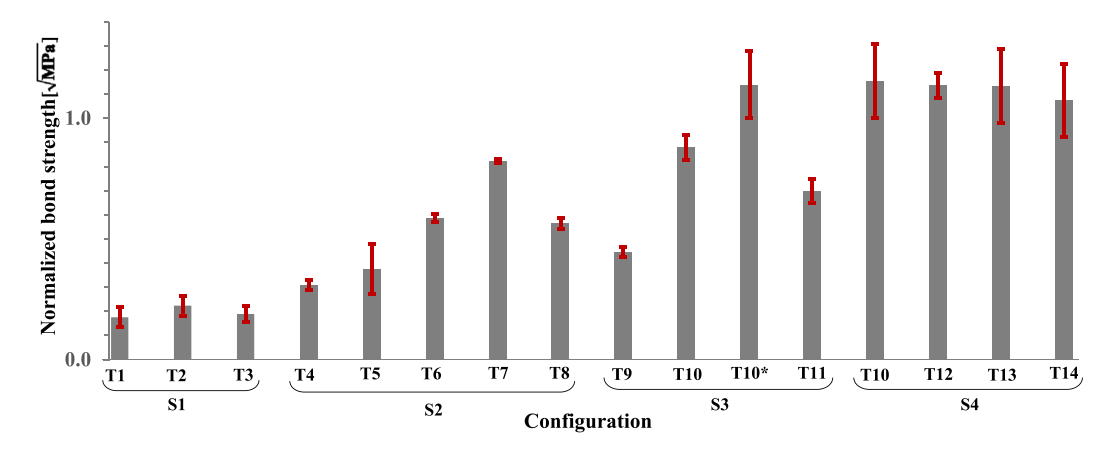


Fig. 15. Mean value and standard deviation of the normalized bond strength for each configuration. (Bond strength normalized by the square root of the concrete compressive strength.).

3.2.2. Series S2: effects of geometric features and surface-roughening treatments

Table 2 shows results obtained for configurations S2T4 to S2T8, designed to investigate the effects of surface and geometry treatments on the bond performance of the plates. As mentioned previously, the majority of the specimens tested within series S2 failed due to bond slip. However, the ribbed specimens, which exhibited the highest nominal bond strength within this series, failed by splitting (see specimens S2T7R1 to S2T7R3 Table 2), suggesting that the measured bond strength represents a lower bound on the actual bond strength offered by ribbed specimens. As is often the case for pullout tests performed on traditional ribbed rebars, the splitting failure observed for specimens S2T7R1 to S2T7R3 is likely to have been induced by the compression forces developed between ribs and surrounding concrete. When ribbed reinforcement slides relative to the concrete, it results in the development of compressive stresses in a radial direction and tensile stresses in a circumferential direction within the concrete. If the amount of concrete surrounding the reinforcement is relatively low, or if the concrete lacks sufficient confinement, the circumferential tensile stresses can lead to cracks that can propagate throughout the entire concrete mass. This sudden propagation of cracks generally results in a significant reduction in bond strength and leads to splitting failure before the reinforcement can be extracted. The full capacity offered by lateral ribs is discussed in detail in the results section dedicated to series 3, where additional tests were designed to achieve slip failure in the presence of lateral ribs.

Table 2 shows that all the bond-enhancing technologies investigated in series S2 significantly improve on the bond performance of the prismatic laser-cut strips studied in series S1, whose average bond stress was of the order of 1 MPa. Specifically, Table 2 shows that surface coating (S2T4), surface roughening (S2T5), perforations (S2T8) and ribs (S2T7) lead to a progressive improvement in bond performance, with average bond strengths of 1.87, 2.23, 3.60 and 4.68 MPa, respectively. This is in line with previous studies on FRP bars, showing that surface roughening can lead to significant increases in bond strength performance [26]. It is also worth noting that when ribs and perforations are adopted simultaneously (S2T8), the bond stress is lower than in the case of ribs and perforations adopted individually (S2T7 and S2T6 respectively). This behaviour might be linked to concrete compaction challenges associated with the simultaneous presence of ribs and perforations. These bond strength results, graphically summarized in Fig. 9(b), indicate that the proposed LCR technologies can be ranked based on their bond performance as follows: (i) ribs, (ii) perforations, (iii) ribs and perforations, (iv) surface roughening, and (v) steel prime coating.

Fig. 12 presents the bond stress-slip behaviour for slips up to 20 mm. It is evident from this that coated specimens (e.g., S2T4R1) exhibit

similar qualitative behaviour to smooth prismatic plates. That is, the prime coating appears to enhance bond performance without causing any significant changes in bond mechanisms. On the other hand, roughening, perforations and ribs seem to significantly alter the bond stress-slip behaviour. In particular, surface roughening (e.g., S2T5R1) leads to a non-smooth post-peak softening behaviour, with the curve exhibiting a marked periodicity. This might be representative of actual physical mechanisms that cannot be elucidated via the results obtained in this study. Thus, further dedicated studies are needed to clarify the underlying processes. On the other hand, perforations (S2T6R1) and simultaneous perforations and ribs (S2T8R1) lead to a sudden decrease in bond stresses for slips of the order of 4-5 mm. Although this could possibly be attributed to the development of mechanisms that prevent stress transfer through friction, more research is needed to shed further light on such processes. Fig. 12 also shows that when only ribs are present (S2T7R1), progressive hardening is achieved up until concrete split failure, occurring at a slip of approximately 9 mm. This suggests that, in isolation, ribs provide an additional bond transfer mechanism that is more compliant than steel-to-concrete adhesion, but stiffer than mere friction.

The bond strength CoV obtained for coated, perforated, ribbed and ribbed-perforated specimens is of the order of 7% or lower, demonstrating the relatively low levels of variability associated with the use of these techniques. In contrast, when using surface roughening the bond strength CoV was of the order of 28%. With concrete compressive strength typically exhibiting a CoV of the order of 3%–15% [24], a CoV of 28% indicates a relatively high degree of uncertainty associated with the use of this technique.

3.2.3. Series S3: effects of ribs spacing

As described previously, test series S3 was designed to investigate the effects of rib spacing on bond strength. For all of the configurations studied, slip failure was invoked to assess the actual bond capacity of the plates. The majority of specimens tested within series S3 experienced failure through bond slip. However, as in series S2, ribbed specimens with a rib spacing of 18 mm exhibited premature failure under standard testing conditions; see results reported in Table 2 for configuration S3T10 (specimens S3T10R1 to S3T10R3). Fig. 16 shows examples of split and slip failures (specimens S3T10R and S4T14R respectively). Specifically, Figs. 16(a) and 16(b) show that, when splitting occurs, the split crack originates at the loaded end of the bar, develops in the same plane of the bars, and propagates towards the non-loaded end of the LCR. To invoke slip failure for this particular configuration, series 3 included three additional tests with increased lateral confinement (specimens S3T10R4 to S3T10R6). These tests failed by bond slip (see Figs. 16(c) and 16(d)), demonstrating that the provided confinement prevented the development of radial cracks,

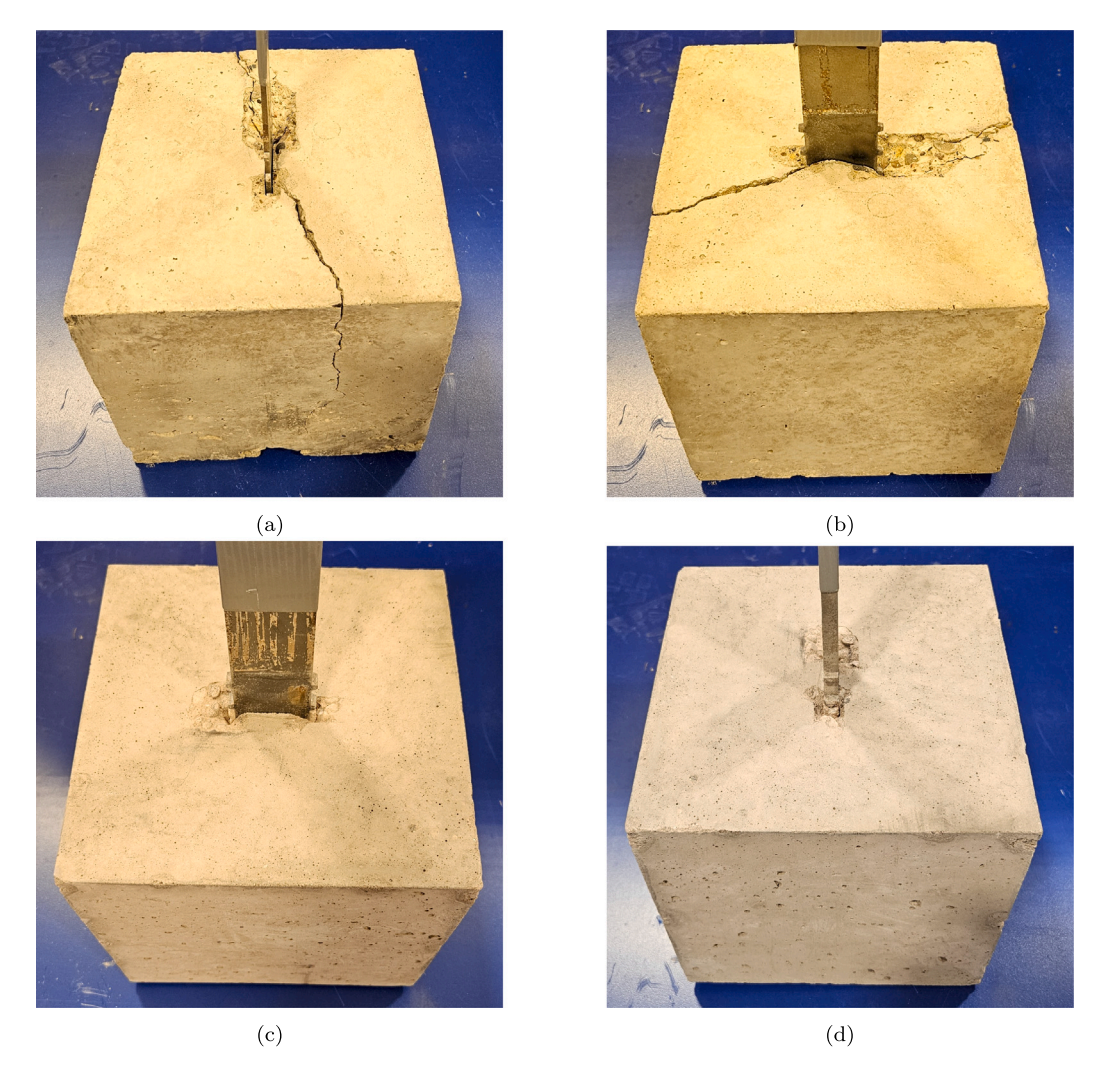


Fig. 16. Split failure of the specimen S3T10R1: (a) lateral and (b) frontal view, and slip failure of specimen S4T14R1: (c) lateral and (d) frontal view.

hence promoting crushing or shearing of the concrete between the transverse ribs [27,28].

Table 2 presents bond strength results for rib spacings of 36, 18, and 9 mm (referred to as S3T9, S3T10, and S3T11, respectively). Among these configurations, specimens with an 18 mm rib spacing provided the highest bond strength, giving an average bond strength of 5 MPa and 6.34 MPa in the case of unconfined and confined conditions respectively. This illustrates that incorporating ribs with an appropriate spacing can enhance the bond capacity by approximately six times compared to smooth prismatic laser-cut reinforcement.

It is evident from Fig. 9(c) that the investigated configurations can be ranked based on their bond performance as follows: (i) 18 mm spacing, (ii) 9 mm spacing, and (iii) 36 mm spacing. Interestingly, these results seem to suggest that decreasing the rib spacing (i.e., increasing the total number of ribs) has a detrimental effect on LCR bond capacity. Although this seemingly counter-intuitive trend could be linked to poor concrete compaction in the areas between adjacent ribs, further studies are needed to confirm the underlying mechanisms.

The bond stress-slip curves presented in Fig. 13 show that all the specimens failing by slip failure exhibit a residual bond stress of the order of 25% of the peak stress, or higher. As expected, specimens failing by splitting exhibited an abrupt decrease in stress values following splitting, resulting in near-zero stress levels for higher values of slip (see for instance the curve reported in Fig. 13 for specimen S3T10R1). However, when lateral confinement was applied, residual bond stresses of the order of 50% of the peak stress were achieved for slip values

between 10 and 20 mm (e.g., see the curve reported in Fig. 13 for specimen S3T10R4), confirming that the introduced stirrups confined the specimens effectively.

3.2.4. Series S4: effects of plate thickness

Series S4 explored how the thickness of LCR affected the bond strength of ribbed plates, which were found to be the most effective configuration among those investigated in series S1 to S3. Table 2 shows that in all twelve specimens in the fourth series (i.e., S4T10, S4T12, S4T13, and S4T14) slip failure was induced as intended, facilitating accurate assessment of the actual bond capacity of the plates. The average bond strength recorded across all specimens ranged from 5.58 MPa to 5.98 MPa, suggesting that bond strength is largely independent of plate thickness; Fig. 9(d) illustrates this graphically. This trend might be explained by the fact that (i) the thickness of the plates has minimal influence on the overall lateral surface available to generate chemical bond and friction stress, and (ii) the thinnest plate considered in this study is still thick enough not to induce punching failure of the concrete surrounding the ribs, hence allowing full development of interlocking mechanisms.

In all stress-slip curves presented in Fig. 14 significant levels of residual bond stress can be observed after the peak bond stress had been reached. In particular, all specimens developed residual bond stresses exceeding 50% of the peak stress for slip values between 10 and 20 mm. This behaviour is qualitatively similar to that observed in series S3 for ribbed plates tested under confined conditions (see e.g., the curve

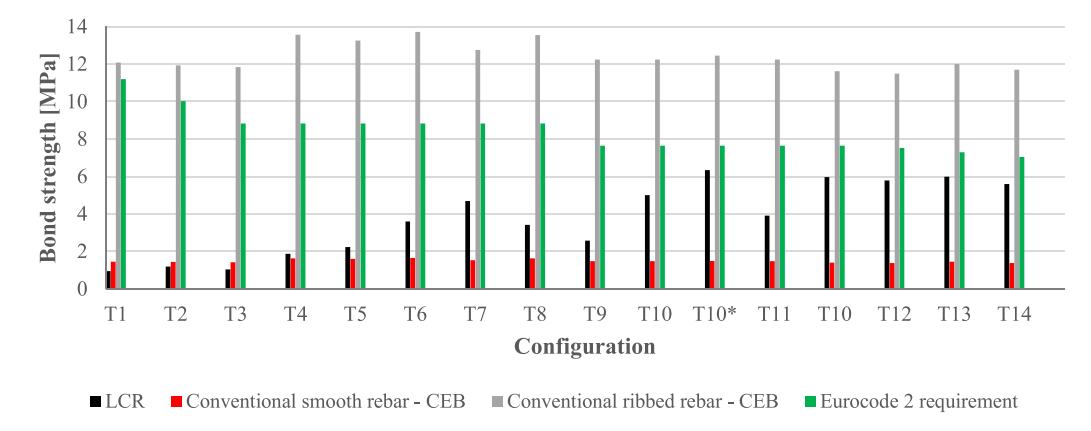


Fig. 17. Comparison between: (i) the experimentally measured bond strength of LCR, (ii) the bond strength of conventional smooth and ribbed rebars evaluated through the CEB FIP Model, and (iii) the minimum bond strength required by Eurocode 2 for standard reinforced concrete applications (Eq. (1)).

obtained for S3T10R4 reported in Fig. 13). The relatively high levels of residual stress recorded for these specimens can be attributed to the effects of confinement, which underpins interlocking and friction mechanisms following debonding between LCR and concrete.

3.3. Bond capacity of LCR and conventional rebars

To assess the bond capacity of LCR in comparison to conventional rebars, here the use of established empirical formulas, widely used to evaluate the performance of conventional rebars, is considered. Additionally, the experimentally determined capacity of LCR is compared to the minimum bond capacity required by Eurocode 2 for standard applications, considering traditional reinforcement with an equivalent cross-sectional area.

Many empirical formulae have been presented in the literature to assess the bond capacity of conventional rebars (e.g., [29–37]). These include formulae which estimate bond strength as a function of concrete compressive strength (e.g., [33,35,38]). Over the years, these formulae have been refined by incorporating additional factors, such as rebar diameter, concrete cover, and the ratio of bonded length to rebar diameter, in an effort to enhance the predictive capabilities of the proposed models [36,37,39,40].

To assess the capacity of traditional rebars, this work employs the CEB FIP Model [25], which uses a widely accepted, simple and well-validated relationship to assess the bond capacity of traditional rebars as a function of the concrete compressive strength. For instance, a comprehensive validation study for this model is available in Heskett et al. [41]. The CEB FIP Model adopted here proposes the function $2.5\sqrt{f'_c}$ to estimate the bond strength of ribbed rebars, while the expression $0.3\sqrt{f'_c}$ is recommended for smooth rebars. Note that, in the above expressions, f'_c is the compressive strength derived from concrete cylinders.

In parallel, the minimum bond strength required by Eurocode 2 for conventional rebars of equivalent cross-sectional area is calculated as follows [42]:

$$\tau \ge 0.098 (130 - 1.9\phi) \tag{1}$$

where τ is the bond strength and ϕ is the bar diameter.

Fig. 17 graphically compares (i) the bond strength of LCR determined experimentally, (ii) the bond strength of conventional reinforcement, assessed for both smooth and ribbed rebars using the CEB model, and (iii) the minimum bond strength required by Eurocode 2 for conventional rebars of equivalent cross-sectional area. The chart shown in Fig. 17 indicates that the bond strength achieved by smooth prismatic laser-cut strips (configurations T1 to T3) is marginally lower, yet comparable, to the anticipated bond strength of traditional smooth rebars. It can also be observed that all of the bond-enhancing features introduced in the other configurations (T4 to T14) lead to a higher bond

strength in comparison to smooth rebars. On the other hand, Fig. 17 demonstrates that all the configurations studied in this research exhibit a lower bond strength in comparison to ribbed rebars. Specifically, the obtained LCR bond strengths vary between 7.8% (for configuration T1) and 51.3% (for configuration T10) of the expected bond strength for ribbed rebars. Similarly, the figure shows that all of the configurations develop a lower bond strength than the minimum required according to Eurocode 2. The bond strength obtained varies between 8.5% (for configuration T1) and 82.9% (for configuration T10) of the minimum bond strength required as per Eq. (1).

The results presented in Fig. 17 suggest that, in most cases, the bond performance of the examined LCR is bracketed by the bond strength of conventional smooth and ribbed rebars. The comparison with the minimum required bond strength required by Eurocode 2 suggests that the examined LCR configurations do not meet the stated requirement for traditional reinforcement. Although no configuration strictly meets the Eurocode requirement for individual bars, the bond strength of ribbed LCR specimens approaches the requirement, indicating that minor improvements through further optimization are likely to allow their direct use for standard applications. Additionally, it should be noted that one of the key benefits of LCR is that, if the plates are assembled in reinforcement cages with effective steel-to-steel joints, they are likely to do develop adequate anchorage to the concrete through e.g., hook mechanisms.

4. Numerical modelling of the bond behaviour of ribbed plates

This section presents a numerical study to elucidate the stress transfer mechanisms associated with the best-performing configuration examined in this study, namely ribbed LCR plates (S3T10). The aim of this section is twofold: to observe mechanisms that are not directly detectable via experimental tests and to develop a validated numerical framework for the preliminary design of LCR. To achieve mechanism-based modelling, this section combines the effects of chemical adhesion, frictional forces, and mechanical interlocking specific to ribbed LCR plates.

4.1. Numerical modelling

4.1.1. Modelling strategy

Over the years, several numerical approaches have been used to model and analyse the pullout behaviour of steel rebars in reinforced concrete, including Finite Element Analysis (FEA), the Discrete Element Method (DEM) [43], lattice models and cohesive zone models [44,45]. Among these, FEA approaches have been widely used and validated at different scales. For instance, the nonlinear spring method has been successfully employed as a simplified, empirical approach for modelling the bond behaviour between steel bars and concrete at a structural

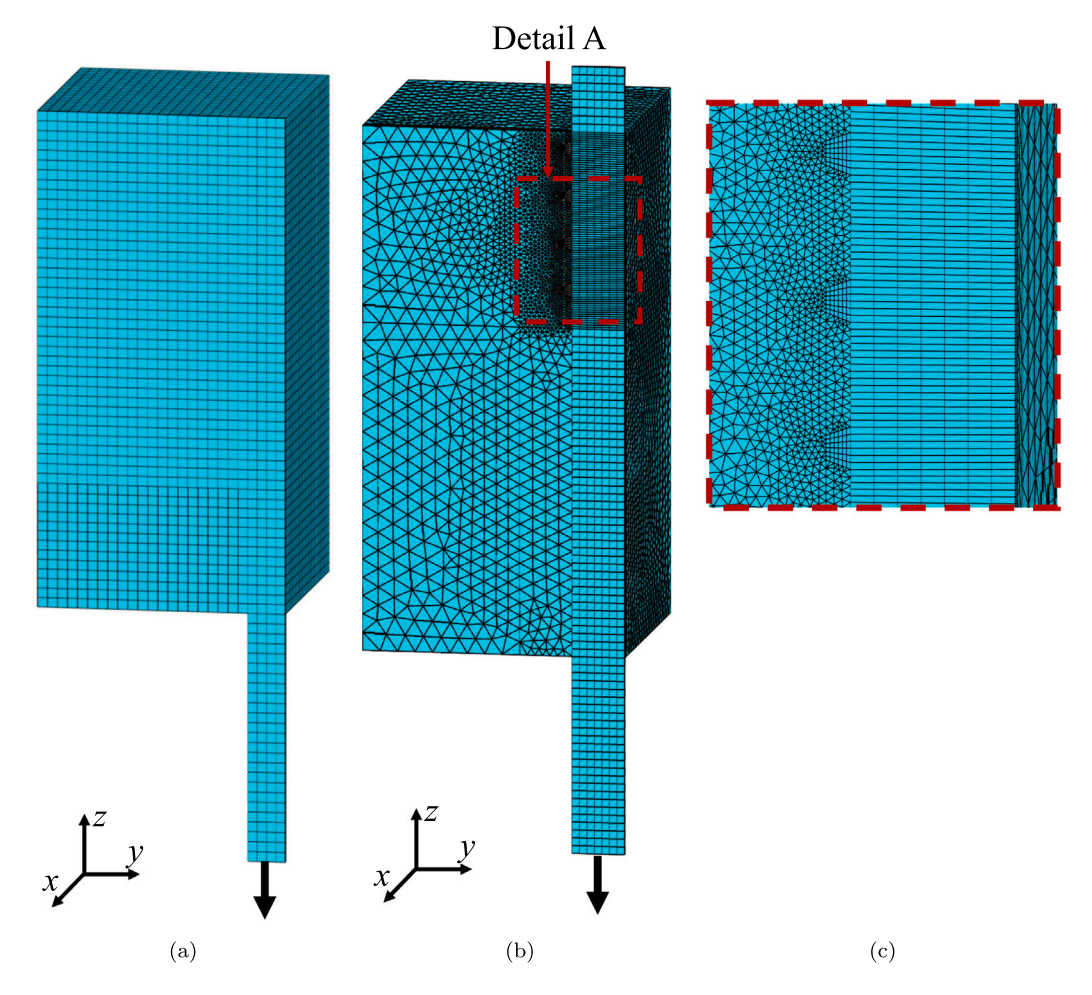


Fig. 18. 3D view of the FE models: (a) prismatic smooth LCR (reproducing configuration S1T3), (b) ribbed LCR (reproducing configuration S3T10), and (c) detail A of the FE mesh for ribbed LCR, illustrating the local mesh refinement adopted for the concrete in close proximity to the ribs.

element scale [46–50]. Similarly, detailed non-linear finite element models have been successfully implemented in a number of studies to assess the mechanisms of bond stress transfer [51,52]. For instance, concrete-damage constitutive models have been successfully employed to simulate concrete deterioration and splitting failure [53]. Zerothickness cohesive elements have also been successfully embedded within the standard finite element mesh representing the bulk materials (steel and concrete) to model the response of the interface to loading and separation [54,55].

To explicitly model the effects of chemical adhesion, friction, and mechanical interlocking, this study builds on the aforementioned studies and employs a combination of concrete-damage models and cohesive surfaces. Specifically, (i) cohesive surfaces are employed to capture the shear behaviour of concrete-to-steel interfaces, thus modelling the effects of chemical adhesion and friction, and (ii) a concrete damage-plasticity model is adopted to capture concrete cracking and crushing, modelling the effects of concrete-rib interlocking in the bulk concrete material. A detailed description of the finite element model is provided in the following section.

4.1.2. Finite element modelling

The mechanisms underlying the bond behaviour of ribbed LCR are here studied through finite element models that seek to reproduce pull-out tests involving both prismatic and ribbed LCR plates. First, a model of the pullout test on a smooth prismatic laser-cut strip (configuration S1T3, see Table 2 and Fig. 3) was developed to validate the shear response of the adopted cohesive surfaces; see FE mesh depicted in Fig. 18(a). As this configuration does not involve ribs, it allowed the

combined effects of chemical adhesion and friction to be modelled and validated in isolation, i.e., in the absence of mechanical interlocking between ribs and concrete. A model of a pullout test on a ribbed LCR plate was then developed to numerically evaluate the combined effects of chemical adhesion, friction and interlocking between the ribs and the surrounding concrete; see Figs. 18(b) and 18(c).

For both models, the LCR plates and surrounding concrete cube were modelled in 3D. To limit the computational cost of the models, only a quarter of the set-up was modelled, taking advantage of the symmetry of the problem (as shown in Fig. 18). Both concrete and steel were modelled using solid elements; hexahedral elements (C3D8) were used for the steel, while tetrahedral elements (C3D10) were used for the concrete to achieve a smooth mesh refinement in close proximity to the ribs, where higher strain gradients were expected to develop. The required level of mesh refinement was established through a preliminary mesh sensitivity study. As mentioned in the previous section, the shear behaviour of the concrete-steel interface was modelled through cohesive surfaces between the solid elements used for concrete and steel. To model the reaction offered by the steel plate located at the bottom of the test setup (see Figs. 2 and 7), all nodes belonging to the bottom face of the concrete cube were prevented from moving in the vertical direction (i.e., along the z-axis in Fig. 18). Additionally, to reproduce the effects of lateral confinement offered by the steel stirrups in tests S3T10R4 to S3T10R6, in the ribbed LCR model the lateral faces of the concrete cube were prevented from moving in their normal direction. As represented in Fig. 18, a gradually increasing pullout force was applied in direction -z to reproduce the tensile force generated when using the testing apparatus.

The material behaviour of concrete was modelled using the wellvalidated Concrete Damage Plasticity (CDP) model [56], where the input parameters are stress-strain curves in tension and compression. These curves were derived through the empirical model presented in [25], based on the average compressive strength and the maximum aggregate size of the mix used in the present study. Based on the grade of steel used in the tests (\$355), the steel was modelled as an elastic perfectly-plastic material with Young's modulus of 210 GPa, Poisson's ratio of 0.3, and yield stress of 355 MPa. Cohesive behaviour with linear softening was defined for the interface surfaces. The driving input parameters were derived from experimental measurements performed in the present study. Specifically, a nominal maximum shear stress of 1 MPa was assigned as the shear damage initiation criterion based on the bond strength observed for the S1T3 specimens (Table 2). Similarly, a unit-surface fracture energy of 0.06 N/mm was assigned to the cohesive surfaces. Such a value was estimated as a function of the average concrete compressive strength measured in this study, using the empirical CEB FIP model [25]. The friction effects on the tangential behaviour were represented using the Coulomb friction model [57], selecting a friction coefficient of 0.35, from [58]. Normal behaviour was assumed to be perfectly rigid.

The numerical simulations were carried out using the finite element package Abaqus [59]. To capture the geometrically non-linear behaviour of the system, the models were solved for large deformations. Numerical solutions were obtained using the explicit solver. To prevent inertial effects affecting the results, which can occur when solving problems using an explicit (i.e., time-stepping) solution strategy, the loads were applied quasi-statically. Specifically, a displacement rate of 1 mm/sec was applied to the loaded end of the LCR.

4.2. Numerical results

The results obtained when smooth prismatic LCR was modelled are summarized in Fig. 19. Fig. 19(a) shows that, while the experimental stress-slip curves exhibit a non-linear softening branch, the numerically obtained softening branch is approximately linear, owing to the linearsoftening model implemented for the cohesive surfaces. However, the figure also shows that, for slips up to about 3 mm, the numerically obtained stress-slip curve captures the general trend of the experimental results obtained for the three specimens tested. Given that the anticipated slip at the concrete-steel interface in ribbed LCR is consistently smaller than 3 mm, the adoption of a linear-softening model for cohesive surfaces was deemed suitable for examining the combined impacts of chemical adhesion, friction, and mechanical interlocking in ribbed LCR scenarios. To validate such an approach, an analysis of the slip magnitude expected to occur at the interface is included in the discussion of the ribbed LCR model. Fig. 19(b) shows the evolution of damage in the cohesive surfaces for the smooth prismatic LCR model. The figure indicates that cohesive surface damage initiates at the loaded end of the bonded region (see state no. 1 in Fig. 19(b)) and then propagates towards the free end at higher levels of slip (see states no. 2 to 4 in Fig. 19(b)). This is in line with the experimental observation that the loaded end is mobilized first (see Section 3.2.1), confirming the ability of the model to capture the pullout mechanisms for smooth prismatic LCR. The numerical results indicate that the bulk material remains largely undamaged, thereby confirming that the system's behaviour is primarily governed by the shear behaviour of cohesive elements, driven by chemical adhesion and friction mechanisms.

Fig. 20 presents the results obtained when ribbed LCR was modelled. Due to numerical issues connected with the development of high levels of damage in the bulk concrete for large slips, solutions were only obtained for slips up to 7.4 mm. Fig. 20(a) shows that the numerical simulation approximately captures the trend observed in the experimental tests. Note that, considering the experimental results, the initial slope of the smooth prismatic LCR case (Fig. 19(a)) equals about 60% of that observed in the ribbed LCR case (Fig. 20(a)). This indicates

that, although unable to transfer bond stresses significantly higher than 1 MPa, chemical adhesion and friction mechanisms can significantly contribute to the initial stiffness of the system. An implication of this is that surface treatments aimed at boosting chemical adhesion and friction have the potential to significantly impact the initial stiffness of concrete structures reinforced with ribbed LCR.

In Fig. 20(b), the development of damage in the cohesive surfaces for the smooth prismatic LCR model is illustrated. As seen for the smooth prismatic LCR case, the damage in the cohesive surfaces initiates at the loaded end of the bonded region (state no. 1 in Fig. 20(b)). As slip levels increase, cohesive surface damage propagates towards the free end until the cohesive surfaces are fully damaged (see state no. 2 in Fig. 20(b)). The full development of cohesive surface damage corresponds to a significant change in slope in the stress-slip curve (see region between states 1 and 2 in Fig. 20(a)). Figs. 20(c) and 20(d) show that, when the cohesive surfaces reach a fully damaged state (state 2), the bulk concrete is damaged in limited regions. Specifically, damage in tension (cracking) and compression (crushing) are present immediately above and below each rib, respectively, while relatively large areas of undamaged material are present between ribs. That is, the limited bond stresses that are transferred by chemical adhesion and friction are not inducing any damage in the bulk concrete. This confirms that beyond state 2 (Figs. 20) the main stress transfer mechanism is interlocking. As slip levels increase, damaged areas extend progressively, showing that increasing levels of bond stress are transferred through a stress redistribution process. The results also show that, within the slip range analysed in this study, damage affects a limited region adjacent to the LCR, i.e., it does not propagate throughout the specimen. This confirms the ability of the adopted model to capture the behaviour of confined pullout tests, where slip cracks tend not to propagate across the concrete generating splitting failure.

The results indicate that the shear transfer mechanisms seen in ribbed LCR are similar to those typically observed in traditional ribbed rebars with a circular cross-section (see e.g., [20,40]). At low levels of relative slip, the transfer of shear forces is largely achieved by chemical adhesion and mechanical interlocking. Once the capacity of the chemical adhesion mechanisms is reached, debonding takes place, and stresses are then primarily transmitted through friction and mechanical interlocking. As the slip increases further, mechanical interlocking becomes the dominant mechanism for shear transfer. This suggests that traditional rebars and laser cut reinforcement can be expected to provide comparable tension stiffening, deformations, and crack spacing performance in reinforced concrete members, both in service and in ultimate limit state conditions.

Furthermore, the relatively close agreement observed between experimental and numerical results suggests that the proposed modelling framework can be used with confidence to explore the potential of new configurations, such as different rib geometries, spacings, etc., before conducting mechanical testing (or in conjunction with the latter). For instance, a preliminary assessment of the bond–slip behaviour of prototype LCR geometries can be performed to inform the development of simplified models applicable at larger scales (e.g., as with the spring model). This facilitates comprehensive evaluation of the structural implications of any parameter change before mechanical tests on prototype LCR specimens are conducted.

5. Conclusions

This research contributes to the wider usage of optimized low-carbon Laser-Cut Reinforcement (LCR) by quantifying the bond performance of laser-cut steel and examining its dependence on plate geometry and surface treatment techniques. In particular, the experimental tests allowed the following conclusions to be drawn:

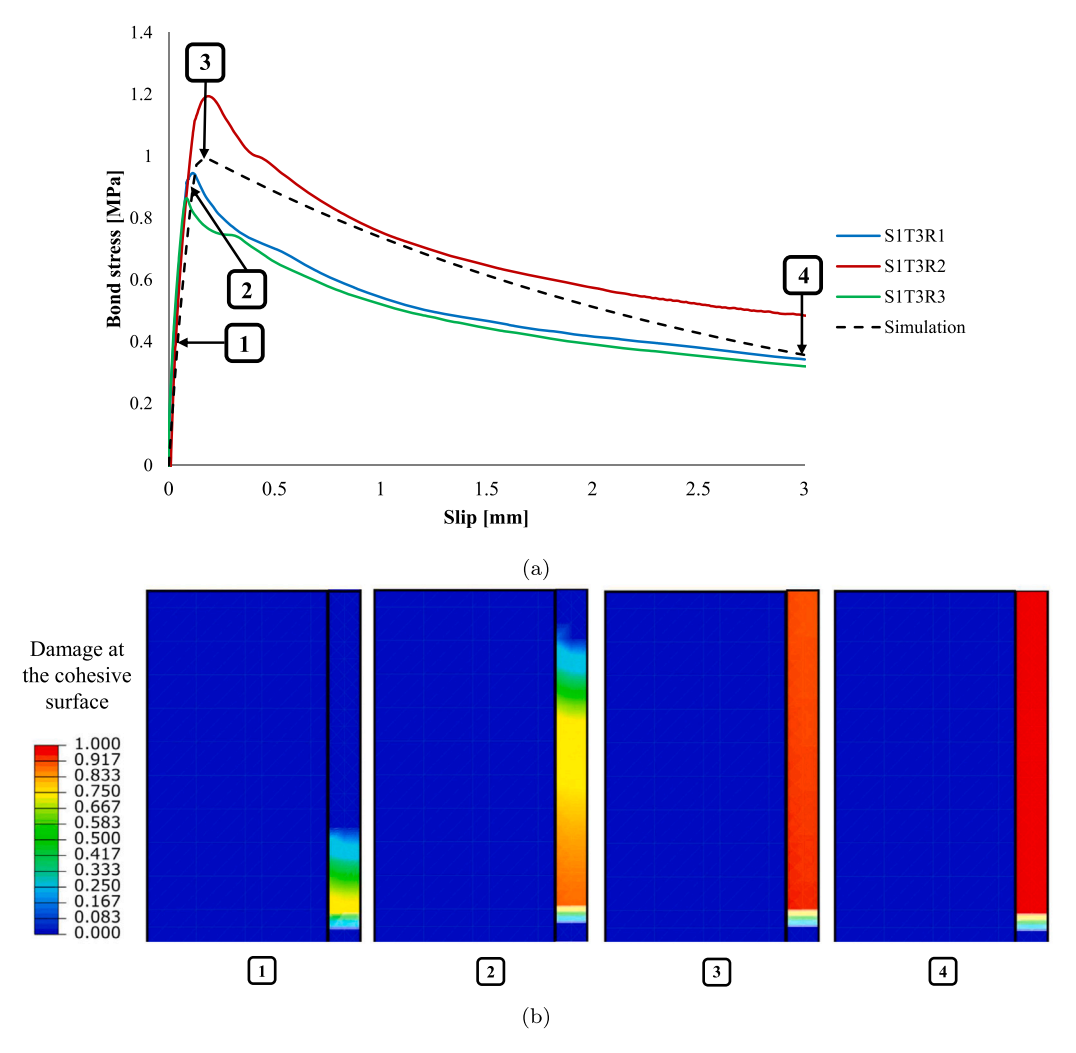


Fig. 19. Numerical model of pullout of smooth prismatic LCR: (a) comparison between numerical and experimental stress-slip curves, and (b) evolution of the cohesive-surface damage at the steel-concrete interface. (Damage results are plotted for a parallel view of the interface, with hidden LCR elements. Results plotted for reference states denoted as state 1 to state 4, corresponding to values of 0.04, 0.11, 0.17 and 3.00 mm, respectively.).

- The width of prismatic laser-cut strips has minimal impact on the bond strength of LCR. Hence, the bond capacity of a particular plate appears to increase approximately in a linear manner with its width, w. This observation can be elucidated by considering that both chemical adhesion and friction provide shear stresses that are roughly proportional to the contact area.
- Ribbed LCR develops significantly higher bond capacity than
 the other geometric features and surface-roughening treatments
 considered in this study. Specifically, the introduction of ribs can
 boost the bond capacity by approximately six times in comparison
 to smooth LCR. The analysed bond-enhancing features can be
 ranked based on their bond performance as follows: (i) ribs, (ii)
 perforations, (iii) ribs and perforations, (iv) surface roughening
 and (v) steel prime coating.
- LCR with a rib spacing of 18 mm exhibited greater bond strength compared to LCR with rib spacings of 9 mm and 36 mm. These results suggest that an optimum rib spacing exists. This trend can be explained by the fact that an excessively small spacing can be linked to poor concrete compaction in the regions between adjacent ribs. Additional research is necessary to verify the underlying mechanisms involved.
- The bond strength of ribbed LCR appears to be independent of plate thickness. The observed trend can be attributed to two factors: (i) the thickness of the plates has minimal effect on the lateral surface available for chemical bond and friction stress

- generation, and (ii) even the thinnest plate considered in the study is thick enough to avoid punching failure of the concrete surrounding the ribs, allowing full development of interlocking mechanisms.
- The bond performance of the tested LCR generally falls between that of conventional smooth and ribbed rebars. Although none of the configurations fully met the Eurocode requirements for bond strength, ribbed specimens came close. This suggests that slight improvements, achieved via further optimization or the adoption of an adequate bonded length, would make them suitable for standard applications. While the tested plates showed relatively low bond strength for traditional structural use, they could be effective in pre-assembled reinforcement cages with steel-to-steel joints, potentially achieving sufficient anchorage to the concrete through hook mechanisms.

Additionally, this work has introduced a numerical simulation framework to gain insights into the mechanisms that influence the bond behaviour of ribbed LCR. The combination of numerical findings and experimental observations have led to the following conclusions:

 Ribbed LCR shares shear transfer mechanisms with traditional ribbed rebars. At low levels of slip, shear forces are mainly transferred through chemical adhesion and mechanical interlocking. When the chemical adhesion reaches its limit, debonding occurs, and stresses are then primarily transmitted through friction

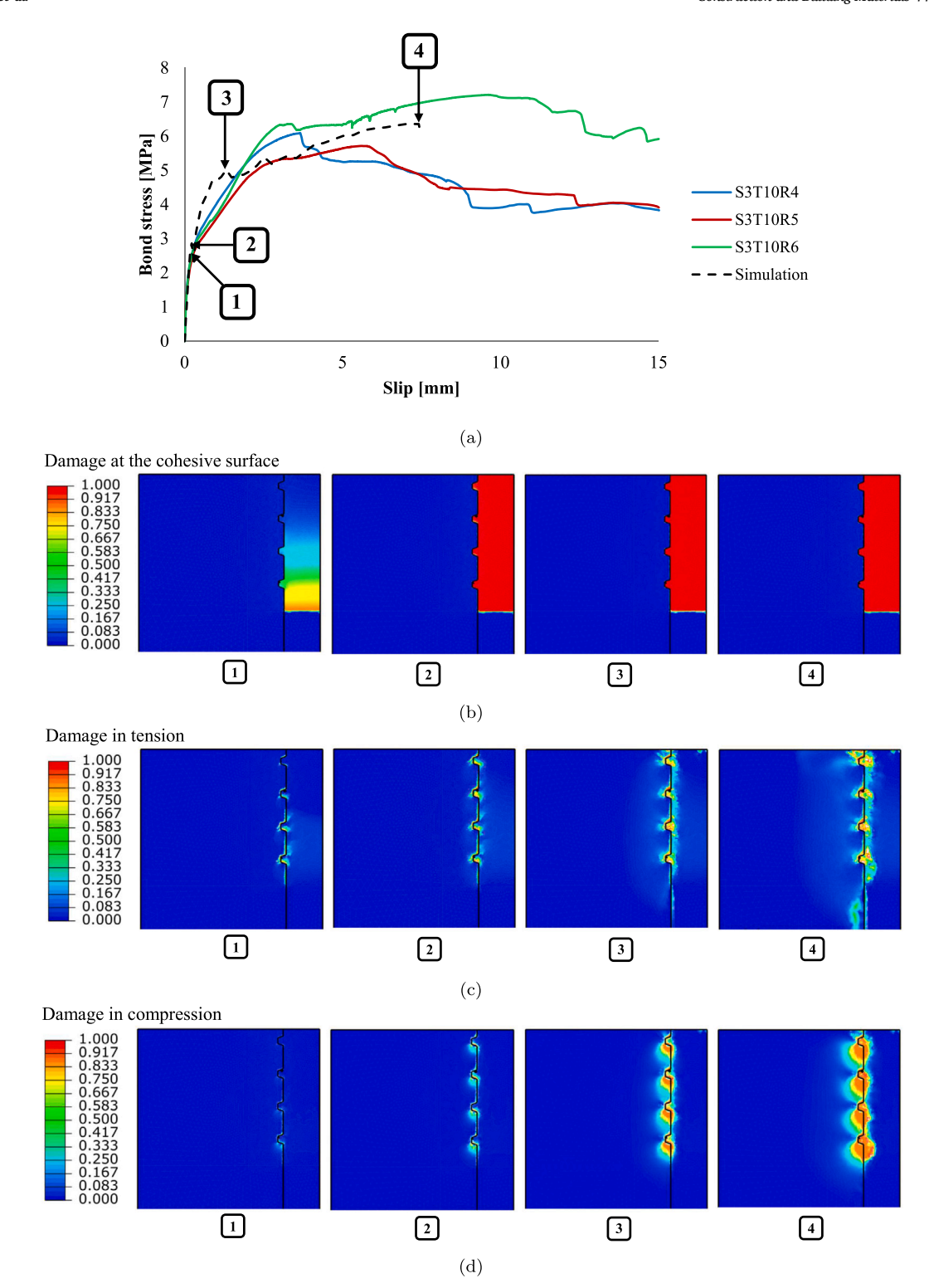


Fig. 20. Numerical model of pullout of ribbed LCR: (a) comparison between numerical and experimental stress-slip curves, (b) evolution of the cohesive-surface damage at the steel-concrete interface, (c) evolution of tension damage in the concrete and (d) evolution of compression damage in the concrete. (Damage results are plotted for a parallel view of the interface, with hidden LCR elements. Results plotted for reference states denoted as state 1 to state 4, corresponding to overall slip values of 0.17, 0.22, 1.32 and 7.44 mm, respectively.).

and mechanical interlocking. With higher slip levels, mechanical interlocking becomes the dominant mechanism for shear transfer. In ribbed LCR, chemical adhesion and friction mechanisms contribute to the initial stiffness of the concrete-to-steel bond. Surface treatments to enhance chemical adhesion and friction can

- thus have a significant impact on the initial stiffness of concrete structures reinforced with ribbed LCR.
- The proposed modelling framework can potentially be employed to explore new configurations before or alongside mechanical testing. Preliminary assessments of bond-slip behaviour can subsequently inform simplified models for larger scales, enabling

thorough evaluation of the structural implications of parameter changes before mechanical testing of prototype LCR specimens.

CRediT authorship contribution statement

Meisam Takalloozadeh: Writing – original draft, Visualization, Software, Methodology, Investigation, Formal analysis, Data curation. Matthew Gilbert: Writing – review & editing, Supervision, Resources, Project administration, Methodology, Funding acquisition, Conceptualization. Dave Allen: Writing – review & editing, Supervision, Conceptualization. Giacomo Torelli: Writing – review & editing, Writing – original draft, Visualization, Validation, Supervision, Software, Methodology, Investigation, Funding acquisition, Formal analysis, Data curation, Conceptualization.

Declaration of competing interest

The authors declare the following financial interests/personal relationships which may be considered as potential competing interests: Giacomo Torelli reports financial support was provided by Engineering and Physical Research Council (EPSRC). Giacomo Torelli reports financial support was provided by European Commission. If there are other authors, they declare that they have no known competing financial interests or personal relationships that could have appeared to influence the work reported in this paper.

Data availability

Data will be made available on request.

Acknowledgements

The financial support of the Engineering and Physical Research Council (EPSRC) for the knowledge exchange project 'Use of optimally placed laser cut steel to accelerate the adoption of low embodied carbon construction materials' is gratefully acknowledged. Giacomo Torelli also acknowledges the financial support provided by the EPSRC, United Kingdom through grant EP/V007025/1 and the EU (European Union) through grant 101123293 (HORIZON-CL5-2022-D4-02), with UK-specific Horizon Europe Guarantee Extension via UKRI grant 10089449. For the purpose of open access, the author has applied a Creative Commons Attribution (CC BY) licence to any Author Accepted Manuscript version arising.

References

- J. Lehne, F. Preston, Making Concrete Change Innovation in Low-carbon Cement and Concrete, The Royal Institute of International Affairs, Chatham House, Great Britain, 2018.
- [2] I.E. Agency, Iron and Steel Technology Roadmap: Towards More Sustainable Steelmaking, OECD Publishing, 2020, URL www.iea.org.
- [3] K. Kwon, D. Kim, S. Kim, Cutting waste minimization of rebar for sustainable structural work: A systematic literature review, Sustainability 13 (11) (2021) 5929.
- [4] S.K. Kim, W.K. Hong, J.K. Joo, Algorithms for reducing the waste rate of reinforcement bars, J. Asian Archit. Build. Eng. 3 (1) (2004) 17–23.
- [5] C.D. Reese, J.V. Eidson, Handbook of OSHA Construction Safety and Health, CRC Press, 2006.
- [6] N. Subedi, Reinforced concrete beams with plate reinforcement for shear, Proc. Inst. Civ. Eng. 87 (3) (1989) 377–399.
- [7] N. Subedi, P. Baglin, Plate reinforced concrete beams: experimental work, Eng. Struct. 21 (3) (1999) 232–254.
- [8] N.K. Subedi, P.S. Baglin, Ultimate load analysis of plate reinforced concrete beams, Eng. Struct. 23 (9) (2001) 1068–1079.
- [9] M.N. Hadi, M.M. Sarhan, L.H. Teh, Behavior of concrete beams reinforced with steel plates, ACI Struct. J. 115 (5) (2018) 1307–1315.
- [10] M.M. Sarhan, M.N. Hadi, L.H. Teh, Bond behaviour of steel plate reinforced concrete beams, Constr. Build. Mater. 189 (2018) 751–756.
- [11] ASTM, Standard Test Method for Comparing Bond Strength of Steel Reinforcing Bars to Concrete Using Beam-End Specimens (A944), ASTM International West Conshohocken, 2015, http://dx.doi.org/10.1520/A0944-22.

- [12] ASTM, Standard Test Method for Bond Strength of Fiber-Reinforced Polymer Matrix Composite Bars to Concrete by Pullout Testing (D7913/D7913M-14), ASTM West Conshohocken, 2014, http://dx.doi.org/10.1520/D7913-D7913M-14R20
- [13] G. Wardeh, E. Ghorbel, H. Gomart, B. Fiorio, Experimental and analytical study of bond behavior between recycled aggregate concrete and steel bars using a pullout test, Struct. Concr. 18 (5) (2017) 811–825.
- [14] M.H. Harajli, B.S. Hamad, A.A. Rteil, Effect of confinement of bond strength between steel, ACI Struct. J. 101 (5) (2004) 595–603.
- [15] W. Zhao, B. Zhu, Theoretical model for the bond-slip relationship between ribbed steel bars and confined concrete, Struct. Concr. 19 (2) (2018) 548–558.
- [16] British Standard, EN 197-1, Cement–Part 1: Composition, Specifications and Conformity Criteria for Common Cements, British Standards Institution, London, 2011, BS EN 197-1:2011.
- [17] British Standard, EN 34-2, Admixtures for Concrete, Mortar and Grout-Part 2: Concrete Admixtures; Definitions, Requirements, Conformity, Marking and Labelling, British Institution Standards, 2009.
- [18] T.H. Kang, S.S. Ha, D.U. Choi, Bar pullout tests and seismic tests of small-headed bars in beam-column joints, ACI Struct. J. 107 (1) (2010) 32–42.
- [19] Rilem-FIP-CEB, Bond test for reinforcing steel: 1-beam test (7-II-28 D). 2-pullout test (7-II-128): Tentative recommendations, RILEM J. Mater. Struct. 6 (32) (1973) 96–105.
- [20] ACI. Committee 408, Bond and Development of Straight Reinforcing Bars in Tension (ACI 408R-03), American Concrete Institute, 2003, p. 49.
- [21] Rilem-FIP-CEB, Bond test for reinforcing steel: 2. Pull-out test, RILEM J. Mater. Struct. 3 (15) (1970) 175–178.
- [22] British Standards, EN 10080:2005, Steel for the Reinforcement of Concrete: Weldable Reinforcing Steel: General, British Standards Institution, 2005.
- [23] B.d.V. Silva, M.P. Barbosa, L.C.P. Silva Filho, M.S. Lorrain, Experimental investigation on the use of steel-concrete bond tests for estimating axial compressive strength of concrete. Part 2: APULOT, IBRACON Struct. Mater. J. 7 (2014) 856–878.
- [24] F.M. Bartlett, J.G. MacGregor, Variation of in-place concrete strength in structures, Mater. J. 96 (2) (1999) 261–270.
- [25] CEB-FIP, Design of Concrete Structures. CEB-FIP Model Code 1990, British Standard Institution, 1993.
- [26] S. Solyom, G.L. Balázs, Bond of FRP bars with different surface characteristics, Constr. Build. Mater. 264 (2020) 119839.
- [27] M.W.T. Mak, J.M. Lees, Bond strength and confinement in reinforced concrete, Constr. Build. Mater. 355 (2022) 129012.
- [28] Y. Zheng, C. Fan, J. Ma, S. Wang, Review of research on bond-slip of reinforced concrete structures, Constr. Build. Mater. 385 (2023) 131437.
- [29] F. Teklal, A. Djebbar, S. Allaoui, G. Hivet, Y. Joliff, B. Kacimi, A review of analytical models to describe pull-out behavior–Fiber/matrix adhesion, Compos. Struct. 201 (2018) 791–815.
- [30] B. Banholzer, W. Brameshuber, W. Jung, Analytical simulation of pull-out tests—the direct problem, Cem. Concr. Compos. 27 (1) (2005) 93–101.
- [31] B. Banholzer, W. Brameshuber, W. Jung, Analytical evaluation of pull-out tests—The inverse problem, Cem. Concr. Compos. 28 (6) (2006) 564–571.
- [32] M. Pecce, G. Manfredi, R. Realfonzo, E. Cosenza, Experimental and analytical evaluation of bond properties of GFRP bars, J. Mater. Civ. Eng. 13 (4) (2001) 282–290.
- [33] R. Eligehausen, E.P. Popov, V.V. Bertero, Local Bond Stress-Slip Relationships of Deformed Bars Under Generalized Excitations, Report, University of California Berkeley, 1982, UCB/EERC 83-23.
- [34] V. Ciampi, R. Eligehausen, V.V. Bertero, E.P. Popov, Analytical model for concrete anchorages of reinforcing bars under generalized excitations, Report, College of Engineering, University of California Berkeley, 1982, UCB/FERC-82123.
- [35] Z. Huang, B. Engström, J. Magnusson, Experimental investigation of the bond and anchorage behaviour of deformed bars in high strength concrete, Report, (94:4) Chalmers University of Technology, 1996.
- [36] A.F. Maree, K.H. Riad, Analytical and experimental investigation for bond behaviour of newly developed polystyrene foam particles' lightweight concrete, Eng. Struct. 58 (2014) 1–11.
- [37] N. Ghazaly, A. Rashad, M. Kohail, O. Nawawy, Evaluation of bond strength between steel rebars and concrete for heat-damaged and repaired beam-end specimens, Eng. Struct. 175 (2018) 661–668.
- [38] M. Harajli, M. Hout, W. Jalkh, Local bond stress-slip behavior of reinforcing bars embedded in plain and fiber concrete, ACI Mater. J. 92 (4) (1995) 343–353.
- [39] A. Shamseldein, H. Elshafie, A. Rashad, M. Kohail, Assessment and restoration of bond strength of heat-damaged reinforced concrete elements, Constr. Build. Mater. 169 (2018) 425–435.
- [40] Y.R. Alharbi, M. Galal, A.A. Abadel, M. Kohail, Bond behavior between concrete and steel rebars for stressed elements, Ain Shams Eng. J. 12 (2) (2021) 1231 1230
- [41] M. Haskett, D.J. Oehlers, M.M. Ali, Local and global bond characteristics of steel reinforcing bars, Eng. Struct. 30 (2) (2008) 376–383.
- [42] B. Standard, EN 1992-1-1:2005, Eurocode 2: Design of Concrete Structures-Part 1–1: General Rules and Rules for Buildings, British Standard Institution, 2005, EN 1992-1-1:2005.

- [43] M. Dehestani, A. Asadi, S. Mousavi, On discrete element method for rebar-concrete interaction, Constr. Build. Mater. 151 (2017) 220–227.
- [44] M. Heshmati, R. Haghani, M. Al-Emrani, A. André, On the strength prediction of adhesively bonded FRP-steel joints using cohesive zone modelling, Theor. Appl. Fract. Mech. 93 (2018) 64–78.
- [45] M. Abbas, B. Bary, L. Jason, A 3D mesoscopic frictional cohesive zone model for the steel-concrete interface, Int. J. Mech. Sci. 237 (2023) 107819.
- [46] C.Y. Li, B. Mobasher, Finite element simulations of fiber pullout toughening in fiber reinforced cement based composites, Adv. Cem. Based Mater. 7 (3–4) (1998) 123–132
- [47] J.-R. Cho, S.Y. Park, K. Cho, S.T. Kim, B.-S. Kim, Pull-out test and discrete spring model of fibre-reinforced polymer perfobond rib shear connector, Can. J. Civil Eng. 39 (12) (2012) 1311–1320.
- [48] F. Yan, Z. Lin, Bond behavior of GFRP bar-concrete interface: damage evolution assessment and FE simulation implementations, Compos. Struct. 155 (2016) 63-76
- [49] M. Mohemmi, V. Broujerdian, P. Rajaeian, An equivalent method for bar slip simulation in reinforced concrete frames. Int. J. Civ. Eng. 18 (2020) 851–863.
- [50] T. Imjai, M. Guadagnini, K. Pilakoutas, Bend strength of FRP bars: Experimental investigation and bond modeling, J. Mater. Civ. Eng. 29 (7) (2017) 04017024.
- [51] Z. Achillides, K. Pilakoutas, FE modelling of bond interaction of FRP bars to concrete, Struct. Concr. 7 (1) (2006) 7–16.

- [52] J. Murcia-Delso, P. Benson Shing, Bond-slip model for detailed finite-element analysis of reinforced concrete structures, J. Struct. Eng. 141 (4) (2015) 04014125.
- [53] G. Barbieri, L. Biolzi, M. Bocciarelli, S. Cattaneo, Size and shape effect in the pull-out of FRP reinforcement from concrete, Compos. Struct. 143 (2016) 395–417.
- [54] S. Khalfallah, Tension stiffening bond modelling of cracked flexural reinforced concrete beams, J. Civ. Eng. Manag, 14 (2) (2008) 131–137.
- [55] A. Caggiano, G. Etse, E. Martinelli, Zero-thickness interface model formulation for failure behavior of fiber-reinforced cementitious composites, Comput. Struct. 98 (2012) 23–32.
- [56] J. Lee, G.L. Fenves, Plastic-damage model for cyclic loading of concrete structures, J. Eng. Mech. 124 (8) (1998) 892–900.
- [57] W.H. Zhou, J.H. Yin, C.Y. Hong, Finite element modelling of pullout testing on a soil nail in a pullout box under different overburden and grouting pressures, Can. Geotech. J. 48 (4) (2011) 557–567.
- [58] M. Beliaev, A. Semenov, S. Semenov, A. Benin, Simulation of pulling the reinforcing bar from concrete block with account of friction and concrete damage, in: MATEC Web of Conferences, Vol. 73, EDP Sciences, p. 04010, http://dx.doi.org/10.1051/matecconf/20167304010.
- [59] Dassault Systèmes, Abaqus analysis user's guide, 2022, URL https://www.3ds. com/support/documentation.